ELSEVIER

Contents lists available at ScienceDirect

# International Journal of Fatigue

journal homepage: www.elsevier.com/locate/ijfatigue





# A two-scale approach for assessing the role of defects in fatigue crack nucleation in metallic structures

Danish Khan <sup>a,\*</sup>, Davide Leonetti <sup>a</sup>, Varvara G. Kouznetsova <sup>b</sup>, Marc G.D. Geers <sup>b</sup>, Johan Maljaars <sup>a,c</sup>

- <sup>a</sup> Department of the Built Environment, Eindhoven University of Technology, P.O. Box 513, 5600 MB, Eindhoven, The Netherlands
- b Department of Mechanical Engineering, Eindhoven University of Technology, P.O. Box 513, 5600 MB, Eindhoven, The Netherlands
- c TNO, Molengraaffsingel 8, 2629 JD, Delft, The Netherlands

# ARTICLE INFO

# Keywords: Defects Crack nucleation Fatigue Notch

# ABSTRACT

Metal structures often exhibit macroscopic defects from which cracks can nucleate during cyclic loading. The current work presents a two-scale approach to enable the prediction of crack nucleation from such defects by taking into account local microstructure features. The geometrical description of the defect and associated non-homogeneous strain fields are modeled using a macroscale model which employs a continuum elastoplastic material model for cyclic deformation. The cyclic deformation of the microstructure near the defect is modeled using a mesoscale model which employs a crystal plasticity material model and uses multiple realizations to address the statistical microstructure variability. The boundary conditions of the mesoscale model are extracted from the macroscale model. By simulating the deformation of the microstructure using the strain fields near the defect and by introducing a fatigue indicator parameter for crack nucleation, along with the weakest-link based upscaling methodology, the developed approach enables the prediction of the distribution of crack nucleation life. The approach is used for analyzing different defects for crack nucleation by considering local grain orientations. The predictions are shown to not only capture phenomena such as scatter, size effects, etc. qualitatively, but also agree with a classical engineering approach and experimentally reported data sets quantitatively.

# 1. Introduction

Engineering metallic structures often contain unintended geometrical discontinuities or imperfections caused by fabrication processes, such as welding. Examples of such imperfections are slag inclusions, under-cuts, and blowholes. In response to the applied load, such imperfections are classical stress raisers [1] that are analogous to an engineering notch in the structure. Under repetitive loading, fatigue cracks can nucleate and grow from these geometrical imperfections leading to fatigue failure. Therefore, in engineering failure analysis, these geometrical imperfections are often called and treated as defects [2,3]. In practice, these defects are of sizes in the order of a couple of millimeters. Hence these defects are macroscopic features in contrast to material microstructural constituents and microscopic material defects, such as non-metallic inclusions and micro-pores. To ensure the safe and prolonged usage of structures containing such macroscopic defects, it is imperative to estimate their fatigue crack

nucleation life  $(N^n)$ . This paper focuses on such macroscopic defects (hereafter simply called defects) and the associated  $N^n$ .

Traditionally, total fatigue life  $(N^F)$  is understood to consist of a crack initiation life  $(N^I)$  and a crack propagation life [4,5]. The value of  $N^I$  is subjective to the crack-length criterion that is used to denote the crack initiation. Typically, an observation of a crack grown to a size of the order of 0.5 mm to 2 mm is used to estimate  $N^I$  [6]. For most engineering metals and alloys, this crack size is much larger than the underlying microstructural features. With the advent of sophisticated crack detection and crack size measurement techniques [7], it has become possible to analyze cracks at smaller crack lengths. This has led to an understanding wherein the traditional definition of initiation is viewed to be further composed of different stages of crack nucleation, microstructurally short crack growth, and physically short crack growth [8–11]. Among these stages, crack nucleation refers to the development of a crack in the nucleant phase, of a size in the order of the characteristic microstructure feature, such as a grain [12–14]. Some

E-mail addresses: d.i.khan@tue.nl (D. Khan), d.leonetti@tue.nl (D. Leonetti), v.g.kouznetsova@tue.nl (V.G. Kouznetsova), m.g.d.geers@tue.nl (M.G.D. Geers), j.maljaars@tue.nl (J. Maljaars).

<sup>\*</sup> Corresponding author.

List of Symbols	
$\sigma$	Stress Tensor.
$\sigma^{dev}$	Deviatoric part of $\sigma$ .
X	Backstress tensor.
$X^{dev}$	Deviatoric part of $X$ .
$\bar{\epsilon}^{pl}$	Equivalent plastic strain.
$\bar{\varepsilon}_{max.M}$	Cycle maximum value of volume-averaged
mux,m	principal strain over the volume $v_M$ .
$ar{arepsilon}_{min,M}$	Cycle minimum value of volume-averaged
,	principal strain over the volume $v_M$ .
$\chi^{lpha}$	Backstress on a particular $\alpha$ th slip system.
$arDelta \gamma_N^lpha$	Slip-range for $\alpha$ th slip system and $N$ th load
	cycle.
$\Delta \vec{d}_m(\vec{x}_m^n)$	Amplitude displacement vector used for
	defining boundary condition at $\vec{x}_m^n$ .
$\dot{\gamma}^{\alpha}$	Slip rate on a particular $\alpha$ th slip system.
γ̈́。	Reference slip rate.
$\dot{s}^{\alpha}$	Rate of evolution of slip resistance.
$\mathbb{E}[Y]$	Mean value of Y.
$\mathbb{V}[Y]$	Coefficient of variation of Y.
$\mu^{\circ}$	Gumbel parameter for $P^{\circ}$ .
ρ	Local root radius of the defect of a semi-
	elliptical cylinder shape.
$\sigma_f'$	Fatigue strength coefficient.
$\sigma_{n,N}^{\alpha}$	Peak normal stress for $\alpha$ -th slip system and
	for N-th loading cycle.
$\sigma^{\circ}$	Gumbel parameter for $P^{\circ}$ .
$\sigma_A$	Applied stress in macroscale model.
$\sigma_{cyc}$	Cyclic Yield Stress.
$\sigma_{y \circ}$	Yield stress at $\bar{\varepsilon}^{pl} = 0$ .
$\sigma_y$	Yield stress at a particular $\bar{\epsilon}^{pl}$ .
$ au^{lpha}$	Resolved shear-stress on a particular $\alpha$ th
Orr. 1	slip system.
$\Theta^r[n_g]$	Orientation-set for $n_g$ number of grains, where each orientation is expressed in terms
	of Rodriguez vector.
$oldsymbol{arepsilon'_f}$	Fatigue ductility coefficient.
,	Effective strain amplitude for theory of
$\epsilon_{eff}$	critical distance.
$\vec{d}_{avg,m}(\vec{x}_m^n)$	Average displacement vector used for defin-
u∪g,m∨ m'	ing boundary condition at $\vec{x}_m^n$ .
$\vec{d}_{max,M}(\vec{x})$	Displacement vector at the peak applied
776675,172	stress, of a point with position vector $\vec{x}$ in
	the macroscale FE model.
$\vec{d}_{max,m}(\vec{x})$	Displacement vector at the peak applied
	stress, of a point with position vector $\vec{x}$ in
	the <i>mesoscale</i> FE model.
$\vec{e}_x, \vec{e}_y$	Cartesian unit base vectors in the plane of
→,,	the macroscale model.
$\vec{x}_{2D,m}^n$	2D projection of $\vec{x}_m^n$ in the plane of the macroscale FE model.
$\rightarrow n$	Position vector of a node at the non-free
$\vec{x}_m^n$	surface with respect to central root point in
	mesoscale FE model.
a	Material parameter for isotropic hardening
	in mesoscale model.
b	Material parameter for isotropic hardening
	in macroscale model.

$b_f$	Fatigue strength exponent.
$c_f$	Fatigue ductility exponent.
$C_{\chi}$	Material parameter for kinematic hardening
λ	in mesoscale model.
$C_{ij}$	Component of Stiffness Tensor at indices
	(i,j).
$C_k$	Material parameter for kinematic hardening
,	in macroscale model.
d *	Average grain size.
$d^*$	Underlying microstructural length scale used to specify the range of values of $L$ .
$D_{\chi}$	Material parameter for kinematic hardening
- χ	in mesoscale model.
$F_Y^{-1}$	Inverse Cumulative distribution function of
•	Υ.
$F_Y$	Cumulative distribution function of Y.
$f_Y$	Probability density function of Y.
$G_k$	Material parameter for kinematic hardening
t.	in macroscale model.
$h_{\circ}$	Material parameter for isotropic hardening in mesoscale model.
$K_t$	Stress concentration factor.
$k_{FS}$	Fatemi-Socie FIP constant.
L	Critical distance
$l_D$	Length of an embedded defect.
$l_v$	Length of $v_m$ .
m	Inverse strain rate sensitivity exponent.
$m_{\circ}$	Exponent in crack nucleation model.
$N^F$	Total fatigue life.
$N^I$	Crack initiation life.
$N_{K_t,l_D}^{n^{\prime\prime}}$	Normalized crack nucleation life for defect characterized with $K_t$ and $l_D$ .
$N_{K_t,l_D}^{n'}$	Normalized crack nucleation life for defect
$K_t, l_D$	characterized with $K_t$ and $l_D$ .
$N^n$	Crack nucleation life.
$N_{K_t,l_D}^n$	$N^n$ for defect characterized with $K_t$ and $l_D$ .
$N^n_{K_t,l_D} \ N^u_{K_t,l_D}$	Unscaled crack nucleation life for defect
	characterized with $K_t$ and $l_D$ .
$n_{\circ}$	Number of $V_m^{\circ}$ in $V_m$ .
$n_g$	Number of grains.  Number of microstructure realizations.
$n_r$ $N_{ss}$	Number of loading cycles for achieving
IV <sub>SS</sub>	stabilized state.
$n_X$	Number of backstresses.
P	$p_{max}$ for whole defect.
$p^{\alpha,g}$	Cycle stabilized value of $p_N^{\alpha,g}$ .
$p_N^{lpha, \mathrm{g}}$	Grain averaged value of $p_N^{\alpha}$ .
$p_N^{lpha}$	Fatemi Socie FIP value for $\alpha$ -th slip system
70	and for <i>N</i> -th loading cycle.
P°	$p_{max}$ in $V_m^{\circ}$ .
$p_{crit}$	Material parameter in crack nucleation model.
$P_{K_t,l_D}$	<i>P</i> for defect characterized with $K_t$ and $l_D$ .
$p_{max}$	Maximum value of $p^{\alpha,g}$ in a grain-agregate.
$q^{\alpha\beta}$	Latent hardening ratio.
$Q_{\infty}$	Material parameter for isotropic hardening
	in macroscale model.

$r_1, r_2$	Radii of a defect of a semi-elliptical cylinder shape.
$R_{\sigma,M}$	Stress ratio in macroscale model.
$R_{\varepsilon,m}$	Strain ratio in mesoscale model.
$s^{\alpha}$	Slip-resistance on a particular $\alpha$ th slip system.
s <sub>o</sub>	Initial slip resistance.
$s_s$	Saturation slip resistance.
$V_M^{\circ}$	Subvolume in $V_M$ serving as independent statistical unit.
$V_m^\circ$	Subvolume in $V_m$ serving as independent statistical unit.
$V_g$	Volume of a grain.
$V_M$	Volume of material in the designated win-
	dow of two-scale approach modeled with <i>continuum</i> treatment.
$V_m$	Volume of material in the designated window of two-scale approach modeled with
	micromechanical treatment.
$v_M$	Counterpart of $v_m$ in macroscale FE model.
$v_m$	Generic defect-root volume element in mesoscale FE model.

researchers also refer to this stage as "formation" [15] and view it to be consisting of the stages of formation of a stable crack embryo and growth to the size of the nucleant [11]. Depending on the applied load, an early crack growth stage of a fatigue crack, such as crack nucleation, can be a considerable portion of  $N^F$  of the material both in smooth and notched conditions [10,16–18].

From the understanding of the physics of fatigue crack formation [19], it is well known that the microstructure of the material plays an important role in the crack nucleation process and causes material-related scatter in  $\mathbb{N}^n$ . Different features of microstructure such as secondary phase particles, inclusions, micro-pores, coarse grains, etc. can govern the crack nucleation process. In the absence of microscopic material defects, for a fairly equiaxed microstructure, the heterogeneous irreversible deformation in grains oriented favorably for slip leads to the formation of persistent-slip bands [6,11,14], which eventually lead to fatigue crack nucleation. Hence grain orientations are one of the important microstructural features in regard to crack nucleation. It has been noted in [20] that the presence of defects enhances the process of crack nucleation, however, the basic microstructural mechanism remains similar to that of without defects. Apart from the local microstructure, an obvious factor governing crack nucleation is the imposed stress or strain field. For a given applied load, the local stresses and strains in the vicinity of defects are higher than in the rest of the structure, with their magnitude depending on the shape and size of the defects and the load applied. Therefore, for a given applied load, both the global driving force, governed by the geometrical characteristics of the defect, and the local driving force, governed by the local microstructure in the vicinity of the defect, are important for the prediction of  $N^n$  in a structure with a defect. This is schematically shown in Fig. 1. It is important to highlight that while the definition of  $N^n$  is founded fundamentally in terms of microstructure, in traditional engineering approaches and practice, the crack-lengthbased criterion of  $N^{I}$  is used for characterizing the early fatigue crack growth behavior. In this paper, the crack growth characteristics, when estimated from traditional engineering approaches and experiments, are discussed using traditional definitions of  $N^I$  and  $N^F$ .

In engineering approaches, defects are treated like notches [21] for the prediction of fatigue life. Local stress and local strain-based approaches are used, along with empirical corrections or notch-root

stress-strain state approximation methods, to estimate the crack initiation life from such geometrical discontinuities [5,22,23]. The local stress-based approach typically uses fatigue strength reduction factor, calculated from formulae such as those given by Peterson [24] and Neuber [25], along with S-N curves obtained using smooth specimens, to estimate the fatigue life of notched/defected components under both finite life and infinite life conditions [26]. On the other hand, the local strain-based approach uses local strain history at the notch root along with the material strain-life curve to predict crack initiation life [22]. To take the local plasticity effect into account, linear elastic solutions of strain-state at notches are modified by plasticity corrections using approximation formulae such as those given by Neuber [27] and Molski and Glinka [28]. However, due to their empirical nature, both localstress and local-strain-based methods have their limitations in terms of applicability to different deformation conditions e.g. sharp notches, where these approaches tend to be very conservative [22,29,30]. To address this and other shortcomings, other approaches such as critical distances [31], highly stressed volume approach [32], stress-gradient approach [33], etc. are used. A review of such approaches is given in [34]. Although the above-discussed approaches are easy to use in a practical setting, they rely on empirical and correction factors that take into account experimentally observed phenomena such as size effects. scatter, etc., but which do not address the underlying responsible factors, among which microstructural heterogeneity is a prominent one. Microstructural heterogeneities can behave differently in different deformation conditions existing in the vicinity of different defects. For example, the probability of crack nucleation in a grain oriented suboptimally for slip and located at the defect root will be higher in the case of a sharp defect than a shallow defect. Such an interaction of microstructural heterogeneities with imposed non-homogeneous strain fields can affect the distribution of crack nucleation life. Traditional approaches do not address such details, but introduce the scatter in fatigue life as an aleatoric uncertainty either in the material parameters or in the initiation life [35–37]. This approach may not be generalizable to different load values, defect shapes, and material characteristics such as local texture in the vicinity of the defect. To include these aspects, the underlying microstructure description should be a part of the fatigue model, for which crack nucleation can be used to denote the early crack growth stage.

A plethora of crack nucleation life models exist that take into account the microstructural descriptors with varied degrees of complexity. For example, some analytical models take into account simple 1-D microstructure descriptors such as grain size, slip band size, or a dislocation pile-up size in the prediction of crack nucleation life. A brief review of such models is presented in [19,38,39]. Other numerical models address crack nucleation with more complex microstructure descriptions (2-D and 3-D) at different length scales [39-43]. In the context of this work, of particular interest are the crystal plasticitybased finite element (CPFE) models for cyclic loading of the material. A general review of these models used for fatigue is presented in [10,44, 45]. Such models take into account the microstructure of the material (often 3-D) in a finite element (FE) modeling scheme via statistical or representative volume elements (RVE), along with the crystallographic orientations of individual grains. Using such a model, Manonukul and Dunne [46] introduced a simple crack nucleation criterion based on the accumulated slip, which enabled them to predict the fatigue crack nucleation life in a nickel alloy in the conditions of both gross and local plasticity. Similarly, Shenoy et al. [47] used a statistical volume element based CPFE model along with the concepts of fatigue indicator parameters (FIP) to study the crack nucleation and microstructural small crack growth in IN100 superalloy. These models are usually used to study the fatigue response of material with a primary focus on the microstructural features. For example, Przybyla et al. [48] used 3D CPFE models to study the influence of primary  $\alpha$  grains in the fatigue response of Ti-6Al-4V. Sharaf et al. [49] studied the influence of the microstructure on the fatigue response of structural steels using 2D

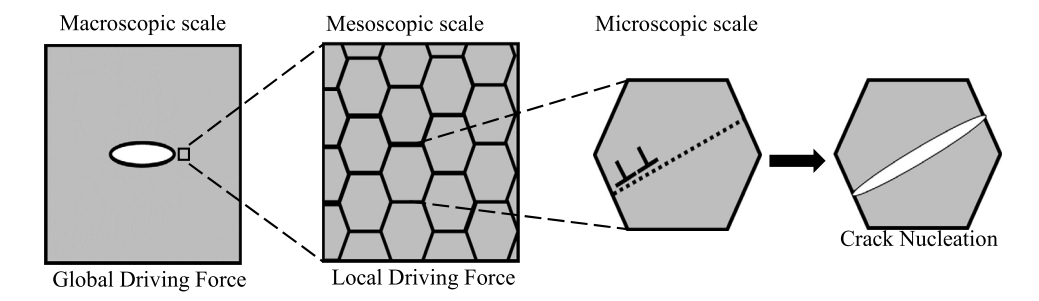


Fig. 1. Crack nucleation near a defect is a multiscale phenomenon. The macroscopic scale governs the global driving force and the mesoscopic scale governs the local driving force for crack nucleation. At the microscopic scale, persistent-slip bands form that lead to crack nucleation.

CPFE models. Since the inherent microstructural variability is captured in these models, some researchers have leveraged this aspect to study its influence on the variability of the fatigue response [50] as well as to include associated size effects [15.51]. Since such models are set up in a FE framework, they can be tailored to study the fatigue response of material in complex deformation conditions. In the past, such models have been used for studying crack nucleation either in pristine microstructures [52,53] or in microstructures with microscopic defects [54,55], where macroscopically homogeneous deformation boundary conditions (BC) can be assumed in the model. A very limited number of studies have attempted to use such models for studying crack nucleation in engineering structures [56] or from engineering-scale (or macroscopic) defects and notches [57-60]. The computationally intensive nature of such models, along with the difference in length scales involved, is a major factor that restricts their usage in such cases. For such applications, it makes sense to use a two-scale approach, which employs two different but coupled models at different length scales [43]. Such an approach can take into account the microstructural heterogeneities at the mesoscale in one model and the non-homogeneous smooth strain fields at the macroscale in another model, without being computationally costly. Although there have been few attempts at using a two-scale approach to analyze specific cases of crack nucleation from holes using 2-D RVEs [55,61], to the best of the knowledge of the authors, no generalized framework has been presented that can be used to address crack nucleation and associated variability and size effects for defects, taking into account the geometrical shapes of the defect and the local 3-D microstructure description. In comparison to the aforementioned engineering and microstructure-based models, such a generalized framework would be able to capture the interaction of non-homogeneous strain fields arising from the shape of the defect and the underlying microstructural heterogeneities, without relying on empirical corrections and assumed material-related variabilities.

Within this background, this work presents a two-scale modeling approach to compare defects in terms of the associated  $N^n$  values. In terms of the scope of the work, the current study focuses on defects that have a finite local root radius. This is because defects with a local root radius tending to zero are expected to have negligible associated  $N^n$  values. For such defects, other stages of crack growth are more relevant, and hence they are out-of-scope for this work. The outline of this article is as follows: Section 2 gives an overview of the two-scale approach. Thereafter, Section 3 presents the theoretical description of the material and microstructure models used in this work, and Section 4 describes the crack nucleation model. Section 5 gives the details of the case study and FE implementation of the two-scale approach. Section 6 contains the main results of this study and a discussion on them. The article ends with Section 7 in which the key conclusions of the study are summarized.

# 2. Two-scale approach

The two-scale approach developed in this work consists of two models: (1) a macroscopic-scale model, hereafter referred to as the

macroscale model, to address the structure with the defect; (2) a mesoscopic-scale model, hereafter referred to as the mesoscale model, to account for the local microstructure in the vicinity of the defect. The type and the scope of the defects of interest are already discussed in Section 1. In the subsequent paragraphs, the modeling approach and the associated approximations used in this work are motivated based on theoretical concepts, empirical understanding, and practical constraints. Two different ways of analyzing material in a cyclic deformation model of a structure are distinguished here: continuum and micromechanical. The material is treated as homogeneous in the continuum model, whereas the microstructure of the material is explicitly taken into account in the micromechanical model.

Fig. 2a schematically shows a grain-resolved, simple metallic structure, containing a semi-circular defect and undergoing cyclic loading. The fatigue crack nucleation driving force for every grain in this structure is expressed in terms of the FIP, which is a microscopic deformation-associated quantity [9,10,47]. The grain with the highest value of cycle-stabilized FIP ( $p_{max}$ ) is the critical grain that nucleates the crack in the structure. It is obvious that in a structure with a defect, the crack nucleating grain will be located in the vicinity of the defect. Such a potential critical grain is highlighted in red in the inset of Fig. 2a.

The microstructure of a metallic structure is not known apriori but can be described statistically. Therefore, to address the microstructurerelated variability of the fatigue life of the considered structure, it is essential to analyze multiple realizations of its microstructure, described in terms of the distribution functions of the associated microstructural features of interest. Since the analysis of one microstructural realization is independent of another, each realization of the microstructure results in an independent statistical unit. Moreover, since each realization results in a different critical grain and thus a different value of  $p_{max}$ for the defect, therefore  $p_{max}$  for the defect has to be represented by a random, i.e. stochastic, variable P, having an associated distribution that, for a given load, depends on the microstructure and the defect characteristics. This distribution addresses the microstructure-related uncertainty observed in  $N^n$  values of a structure with a defect. The major aim of the modeling approach developed in this work is to estimate the distribution of P for a defect by analyzing multiple realizations of the underlying microstructure.

Formally, the deformation of a critical grain, besides its own orientation, depends on all the grains in the structure, the structure's geometry, and the applied load, as shown in Fig. 2a. This implies that establishing the distribution of P for a defect by analyzing multiple independent statistical units through a cyclic deformation model requires a micromechanical analysis of the whole structure. Such a deformation model is referred to as model construct#1 in Fig. 2a and belongs to the category of Direct Numerical Simulations [62]. However, the computational requirement of such a model is exorbitantly high and often needs petascale and exascale computing resources [62]. Tackling such a problem with more modest computing resources requires approximations. In the following paragraphs, these approximations are discussed.

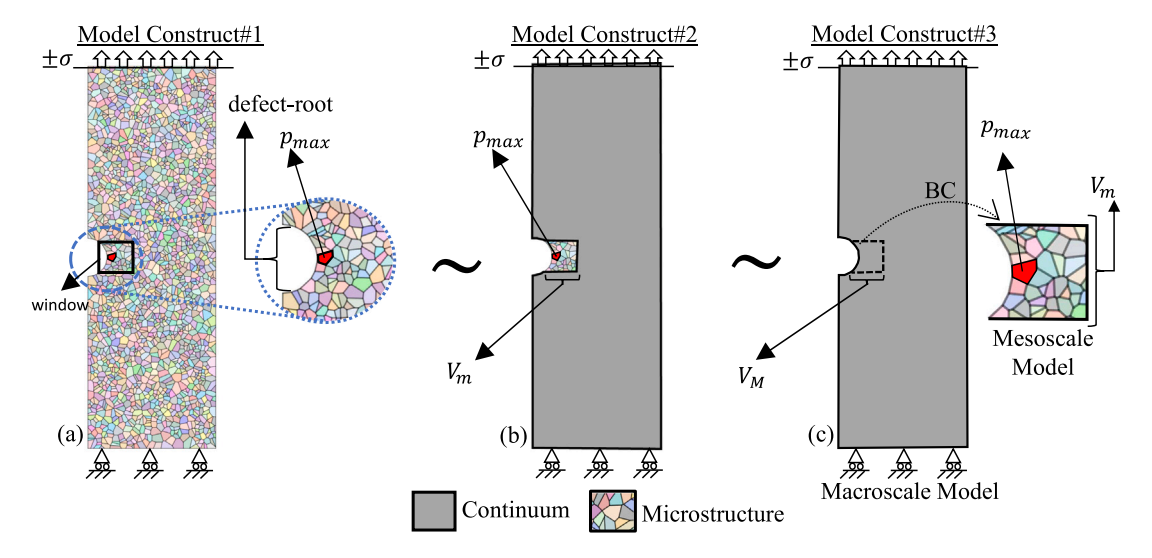


Fig. 2. Crack nucleating grain in a structure with a defect, analyzed using different model constructs: (a) Model construct#1 with only micromechanical treatment of the material. Crack nucleating grain (in red) with FIP value  $p_{max}$  is shown in the inset. The window outside of which the micromechanical treatment of material may be replaced with continuum treatment is also shown. (b) Model construct#2 with the micromechanical treatment of material in volume  $V_m$  of structure and continuum treatment outside it. (c) Model construct#3 with continuum treatment of material in the macroscale model of the structure and micromechanical treatment in the mesoscale model of  $V_m$ , and boundary condition (BC) transfer from  $V_M$  of macroscale to  $V_m$ .

Regarding the dependency of the deformation of a grain on other grains in the structure, it has been shown for homogeneous deformation conditions, that the deformation of a grain depends on the deformation characteristics of its neighboring grains and this dependency decreases with the distance between the grains [63-66]. For non-homogeneous deformation conditions, such as in the vicinity of a defect, the influence of the neighboring grains on the critical grain is expected to be limited to an even smaller grain distance, depending on the local stress gradient of the maximum principal stress along that direction. The steeper the gradient is, the shorter the aforementioned distance. Hence, it can be reasoned that in cyclic deformation analysis of different independent statistical units, for a given remote loading, the actual micromechanical behavior of the material outside a certain window around the root of the defect is not required to estimate the distribution of P. Instead, an average or a continuum treatment of the material can be adopted. As an example, such a window is shown for the defect in Fig. 2a, and the resultant approximate model is shown as Model construct#2 in Fig. 2b. For such a deformation model, the suggested window should satisfy certain size criteria [59,61] to attain the desired level of accuracy. The volume bounded by the window and described with a micromechanical treatment of the material is referred to as  $V_m$ . Model construct#2 belongs to the category of embedded models [61], which have been used in the literature to address different problems [57,59,60]. Although such models are computationally less expensive than the type based on direct numerical simulations, they can still be expensive especially when multiple independent statistical units need to be evaluated. Moreover, such a modeling approach requires the incorporation of different material models, addressing both continuum and micromechanical descriptions of the material in the same modeling domain, which is not possible for some of the open-source FE modeling softwares.

Model construct#3, shown in Fig. 2c, is based on model construct#2 but overcomes some of its limitations. Theoretically, for an independent statistical unit analyzed with model construct#2, the boundary conditions experienced by  $V_m$  depend on the microstructure realization of  $V_m$ , and would vary for each realization. However, if the size of the chosen window (and hence the size of  $V_m$ ) is large enough, an additional approximation can be made that the boundary conditions experienced by the different realizations of  $V_m$  do not vary significantly for microstructure realizations. In Fig. 2c, a model for the cyclic deformation of the structure with a defect, using only a continuum description of the

material, is shown as the macroscale model. The volume of the structure bounded by the window and described with a continuum material model is referred to as  $V_M$ , shown in Fig. 2c. A further approximation can be adopted that during cyclic deformation, the boundary conditions experienced by all possible realizations of  $\boldsymbol{V_m}$  in model construct#2 do not differ significantly from the boundary conditions experienced by  $V_M$  in the macroscale model of Fig. 2c. Therefore, by choosing  $V_m$ of an appropriate size, the boundary conditions for any realization of  $V_m$  can be assumed to be independent of its microstructure realization and can be derived from the continuum analysis of the material. This results in two separate cyclic deformation models at different scales: (1) a macroscale model for the whole structure with only a continuum description of the material, and (2) a mesoscale model of  $V_m$  with only a micromechanical model of the material. To couple the two models, the boundary conditions for the mesoscale model can be obtained from the macroscale model. By modeling the cyclic deformation of  $V_m$ in this two-scale approach, the value of the associated  $p_{max}$  can be approximated, as shown in Fig. 2c. Further, as shown in Fig. 3, multiple independent statistical units can be analyzed by generating multiple mesoscale model realizations for  $V_m$  only. The boundary conditions of each realization follow from the same macroscale model and the associated  $p_{max}$  values can be calculated to retrieve an estimate of the distribution of P for the defect. Such a deformation model can be realized using the technique of submodeling or global-local modeling [67–70]. As described before,  $V_m$  should satisfy certain size criteria to get the desired level of accuracy of distribution of P. Specifically, for this application,  $V_m$  should satisfy two size criteria (SC):

SC1:  $V_m$  is large enough, i.e. contains enough grains, that the distribution of P estimated from it is insensitive to its size [59,61] with a reasonable degree of accuracy.

SC2:  $V_m$  is large enough such that the difference between the average stress–strain response of the material in  $V_M$  and the average stress–strain responses of different realizations of  $V_m$  is small [67–69].

The required size of  $V_m$  for 3-D defects can still be large depending on the dimensions of the defect, resulting in a computationally intensive mesoscale model. However, a statistics-based upscaling approach, similar to the one used by [51,71], can be used to analyze long defects embedded in the bulk of the structures. Fig. 4 shows a portion of the structure with a defect of length  $l_D$ , and its associated  $V_m$ . This defect has the following characteristics:

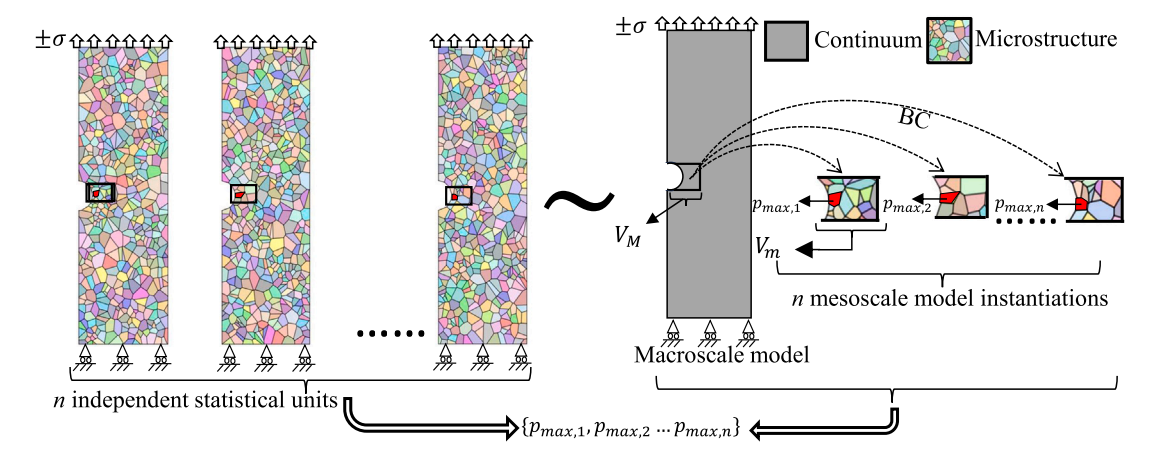
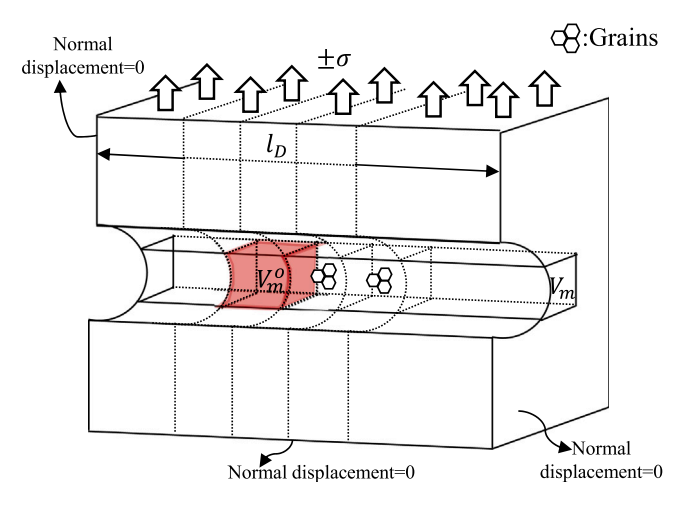


Fig. 3. Estimating the distribution of  $p_{max}$  with model construct#3. Multiple independent statistical units of structure can be analyzed with multiple realizations (instantiations) of the mesoscale model.



**Fig. 4.** Multiple independent statistical unit volumes  $V_m^{\circ}$  in  $V_m$  along the length of a constrained defect  $l_D$ . The grains of one  $V_m^{\circ}$  volume are not affected by the grains of adjoining unit volumes.

- 1.  $l_D \gg d$ , where d is the average grain-size of the material.
- 2. The shape of the defect does not vary much along its length.
- 3. The defect is embedded in the bulk of the structure such that plane-strain deformation conditions can be assumed along the length of the defect.

As shown schematically in Fig. 4, in a two-scale approach for analyzing such a defect, the associated  $V_m$  can be further split along  $l_D$  into smaller equal-size unit volumes:  $V_m^{\circ}$  (with their corresponding  $V_M^{\circ}$  in the macroscale model) such that each unit  $V_m^{\circ}$  complies with the size criteria SC1 and SC2. For such unit volumes, as per SC1, the grains confined in one unit  $V_m^{\circ}$  do not noticeably influence the deformation of grains in adjoining unit volumes, as shown in Fig. 4. Hence each unit  $V_m^{\circ}$  volume in  $V_m$  can be treated as an independent statistical unit and can be analyzed independently using a two-scale approach. Exploiting this scale separation, a two-scale approach has been developed in this work focusing on a single unit volume  $V_m^{\circ}$ associated with such long defect. The macroscale model addresses the cyclic deformation of the full section of the plate containing the  $V_M^{\circ}$ volume with the macroscopic continuum description of the material, whereas the mesoscale model addresses the cyclic deformation of the volume  $V_m^{\circ}$  with a micromechanical description of the material, as shown in Fig. 5. By implementing a two-scale approach for  $V_m^{\circ}$ , the  $p_{max}$  values for  $V_m^{\circ}$  are evaluated, which is represented by the random variable  $P^{\circ}$  having the cumulative distribution function (CDF)  $F_{P^{\circ}}$ .

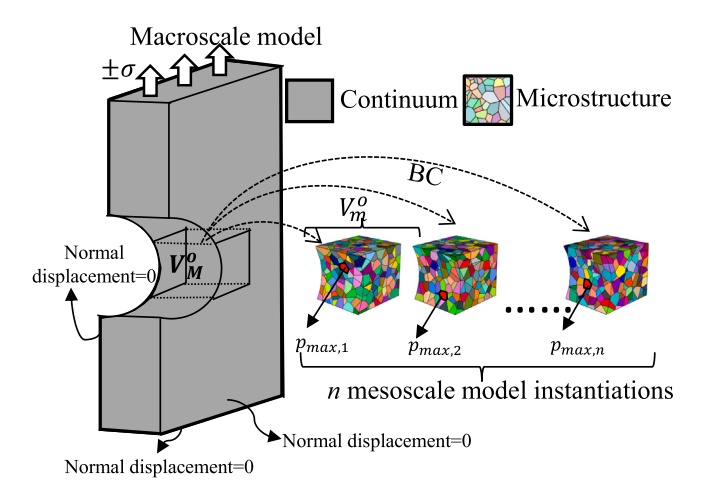


**Fig. 5.** Two scale approach used in this work to estimate the distribution of  $p_{max}$  for  $V_m^{\circ}$  for a structure with a defect, with multiple mesoscale model realizations (instantiations).

Then, using a weakest link approach [51,71], the CDF associated with P, referred to as  $F_P$ , is expressed as:

$$F_P = \left(F_{P^{\circ}}\right)^{n_{\circ}} \tag{1}$$

where,  $n_o$  denotes the number of  $V_m^{\circ}$  volume elements along the length of the entire defect, and is expressed as:

$$n_{\circ} = \frac{V_m}{V_{\circ}^{\circ}} \tag{2}$$

In this way, the distribution of P for embedded defects of different idealized shapes and lengths is approximated through  $F_P$ . Since for a given load,  $V_n^{\circ}$  for a defect is used to characterize the associated distribution of P through Eq. (1), this volume is henceforth termed here as the statistically representative defect-root volume element (DVE). Once  $F_P$  for a defect has been established using a proper choice for the DVE, the associated  $N^n$  values for the defect can be obtained by using a crack nucleation model which expresses a functional dependency between  $N^n$  and P.

# 3. Material and microstructure models

The material analyzed in this work is pure  $\alpha$ -iron. The choice of pure  $\alpha$ -iron as the studied material for this work is based on two arguments: (i) it is crystallographically and compositionally similar to the ferrite phase, which has experimentally been found to be the main

Table 1
Parameters used in the Macroscale Material Model

σ <sub>y</sub> , [MPa]	$Q_{\infty}$ [MPa]	b	C <sub>1</sub> [GPa]	$G_1$	C <sub>2</sub> [GPa]	$G_2$	C <sub>3</sub> [GPa]	$G_3$	C <sub>4</sub> [GPa]	$G_4$	C <sub>5</sub> [GPa]	$G_5$
135	60	7	6.8	360	10.2	359	10.7	359	28.1	1466	133.5	3948

crack nucleating phase in the microstructure of structural steels [49]; (ii) its single-phase nature makes it easier to study than multiphase steel. For this purpose, the material data corresponding to the 99.5% pure  $\alpha$ -iron sample studied by Briffod et al. [55,72], has been used in this work. This material is reported to have an average grain size  $d=35~\mu\mathrm{m}$  without any texture. The cyclic yield stress ( $\sigma_{cyc}$ ) for this material was found to be 273 MPa [73]. The monotonic yield stress of the material is not reported. However, based on the Hall-Petch relation for commercially pure  $\alpha$ -iron given in [74] and the cyclic yield stress monotonic yield stress relation given in [75], the monotonic yield-stress of the material is estimated between 200–250 MPa. The material and microstructure models used in the current two-scale approach are discussed in the following subsections.

### 3.1. Macroscale material model

The cyclic deformation of the material at the macroscale is modeled using a continuum elastoplasticity material model based on von Mises yield criteria and incorporating backstresses. Isotropic elasticity is modeled with Young's modulus of 210 GPa and a Poisson's ratio of 0.33. For plastic deformation, the following expression is used to describe the yield surface:

$$\sqrt{\frac{3}{2}(\sigma^{dev} - X^{dev}) : (\sigma^{dev} - X^{dev})} = \sigma_y$$
(3)

where,  $\sigma^{dev}$  is the deviatoric part of the stress tensor  $\sigma$ ,  $X^{dev}$  is the deviatoric part of the overall backstress tensor X and  $\sigma_y$  is the scalar yield stress at the given equivalent plastic strain  $(\bar{\epsilon}^{pl})$ . The isotropic hardening is modeled by using the Voce-hardening type evolution law for  $\sigma$ ..:

$$\sigma_{\nu} = \sigma_{\nu o} + Q_{\infty} (1 - e^{-b\bar{\epsilon}^{pl}}) \tag{4}$$

where,  $\sigma_{y\circ}$  is the initial yield stress at zero plastic strain and  $Q_{\infty}$  and b are material parameters. The kinematic hardening is modeled using multiple backstresses, where each kth backstress ( $X_k$ ) follows a non-linear hardening evolution law expressed as:

$$\dot{\boldsymbol{X}}_{k} = \frac{C_{k}}{\sigma_{y}} (\sigma - \boldsymbol{X}) \dot{\hat{\boldsymbol{\varepsilon}}}^{pl} - G_{k} \boldsymbol{X}_{k} \dot{\hat{\boldsymbol{\varepsilon}}}^{pl}$$
 (5)

where,  $C_k$  and  $G_k$  are the material parameters and  $\dot{\varepsilon}^{pl}$  is the equivalent plastic strain rate. Finally, the overall backstress tensor is calculated by summing its individual components:

$$X = \sum_{k=1}^{n_X} X_k \tag{6}$$

where,  $n_X$  is the number of backstress contributions.

Such a material model can individually capture cyclic hardening [76] and cyclic softening (as long as the average mechanical behavior remains stable) [77], based on the appropriate choice of isotropic hardening parameters. For this work, the material model parameters for pure  $\alpha$ -iron are taken from the work of Briffod et al. [55], where  $n_X$  is taken as 5. Table 1 shows the material parameters used in this work. The material model is invoked through the commercial FE modeling suite ABAQUS, via the in-built option of combined hardening plasticity. The implementation of the material model is verified by comparing the cycle-stabilized stress–strain curves predicted from the current implementation with the reference simulation results reported in [55].

#### 3.2. Mesoscale material and microstructure model

Given the body-centered cubic (BCC) crystal structure of  $\alpha$ -iron. it has been modeled to deform elastically following cubic elasticity. For accommodating plastic deformation, BCC crystals involve 48 slip systems (three families). However, {110} (111) family of slip systems are often regarded as the primary slip systems at room temperatures for iron and similar materials [78]. For this, and computational reasons, in this work  $\alpha$ -iron is modeled to deform plastically by slip on twelve {110} (111) slip systems. The deformation is modeled using a rate-dependent crystal plasticity model [79] with both isotropic and kinematic material hardening, as implemented in the rate-dependent version of open-source CPFE code PRISMS-Plasticity [80,81], which has been implemented on top of the open-source deal.II [82] C++ FE library. The reader is referred to the publications of the developers of the code [80,81] for a detailed explanation of the implementation of the material model. However, for the sake of completeness, the essential features of the model are mentioned here. The elastic deformation is modeled with Generalized Hooke's law using three independent elastic constants for the stiffness tensor:  $C_{11}$ ,  $C_{12}$  and  $C_{44}$ . For plastic deformation, the slip rate on a particular  $\alpha$ -th slip system  $(\dot{\gamma}^{\alpha})$  is expressed through a flow rule of the form:

$$\dot{\gamma}^{\alpha} = \dot{\gamma}_{o} \left| \frac{\tau^{\alpha} - \chi^{\alpha}}{s^{\alpha}} \right|^{m} sign(\tau^{\alpha} - \chi^{\alpha})$$
 (7)

where,  $\tau^{\alpha}$ ,  $\chi^{\alpha}$  and  $s^{\alpha}$  are the resolved shear-stress, backstress and slip resistance of the slip system, respectively.  $\dot{\gamma}_{\circ}$  and m are the material parameters and refer to the reference slip rate and inverse strain rate sensitivity exponent, respectively. Since all slip systems belong to the same family, therefore they have been modeled with the same initial slip resistance ( $s_{\circ}$ ). To model the isotropic hardening, the rate of evolution of slip resistance on the  $\alpha$ -th slip system ( $\dot{s}^{\alpha}$ ) due to the slip activity on the  $\beta$ -th slip system is given by:

$$\dot{s}^{\alpha} = \sum_{\beta} q^{\alpha\beta} h_{\circ} \left( 1 - \frac{s^{\beta}}{s_{s}} \right)^{a} \left| \dot{\gamma}^{\beta} \right| \tag{8}$$

where,  $h_{\circ}$  and a are the material parameters for hardening and  $s_s$  is the saturation slip resistance of the slip system.  $q^{\alpha\beta}$  is the latent hardening ratio which has a value of 1 when  $\alpha=\beta$  and a value of 1.4 when  $\alpha\neq\beta$  [49,55]. To model the evolution of backstress, Armstrong-Fredrick type [83] nonlinear kinematic hardening law is used, as given by:

$$\dot{\chi}^{\alpha} = C_{\nu}\dot{\gamma}^{\alpha} - D_{\nu} |\dot{\gamma}^{\alpha}| \chi^{\alpha} \tag{9}$$

where,  $C_\chi$  and  $D_\chi$  are material parameters. Similar to the macroscale material model, this material model can capture cyclic hardening [49] and cyclic softening (with stable average mechanical behavior) [77], based on the appropriate choice of isotropic hardening parameters. For this work, the parameters for  $\alpha$ -iron have been taken from the work of Briffod et al. [55] and are given in Table 2.

As discussed in Section 2, the microstructure is described in terms of its microstructural features of interest. In this work, the microstructural feature for studying the microstructure-related variability is the orientations of the grains. Hence for each realization of the microstructure, a unique orientation set of the constituent grains is used. The number of grains in the microstructure captured in the mesoscale model is referred to by the symbol  $n_{\rm g}$ . To model a material with no texture, orientation sets are generated such that the orientations of the individual grains closely conform to a uniform distribution. For this, the sampling technique proposed in [84] is used. This technique results in the generation

Table 2
Parameters used in the Mesoscale Material Model.

C <sub>11</sub> [GPa]	C <sub>12</sub> [GPa]	C <sub>44</sub> [GPa]	γ̈́° [s <sup>-1</sup> ]	m	s。 [MPa]	s <sub>s</sub> [MPa]	h。 [MPa]	a	$C_\chi$ [MPa]	$D_{\chi}$
233.3	135.5	118	0.001	4	60	110	150	2.25	33 000	900

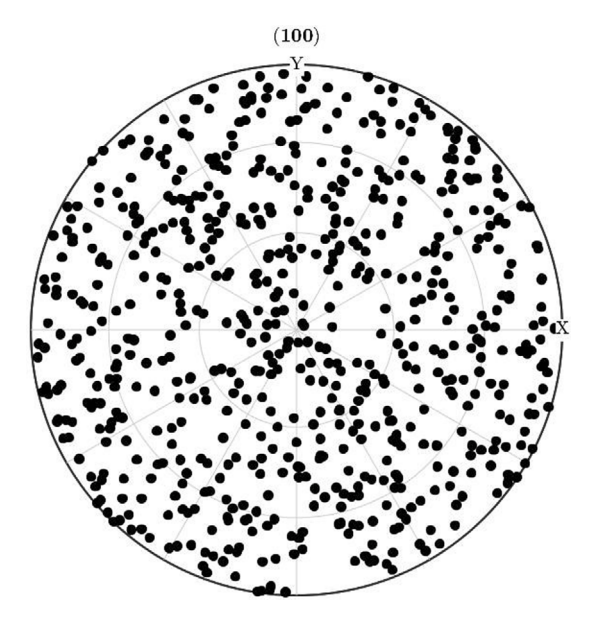


Fig. 6. {100} Pole Figure for one of the orientation sets of 216 grains.

of orientation sets in the Bunge-Euler convention. However, for modeling the deformation of a microstructure realization, PRISMS-Plasticity requires the input of the orientation set of the constituent grains in terms of the Rodriguez vector. For this, another open-source software MTex [85] is used to convert orientation sets from Bunge-Euler convention to Rodriguez vector. The orientation set of  $n_g$  grains when defined in terms of the Rodriguez vector is referred to with the symbol  $\Theta^r[n_g]$ . Using the aforementioned procedure, multiple  $\Theta^r[n_g]$  are generated for multiple microstructure realizations with  $n_g$  grains. As an example, Fig. 6 shows the pole figure associated with one such  $\Theta^r[n_g]$  generated for one microstructure realization with  $n_g = 216$ . The morphology of the grains is another microstructural feature, but, for simplicity, this will not be explored in this work to study the microstructurerelated variability. Hence, a rather simple choice of cuboidal grains with size 35 µm has been used in this work, which remains fixed in the different realizations. Such a cuboidal grain morphology has also been used in the past for modeling the deformation and crack nucleation in materials [58,60,86,87]. Sauzay et al. [88], using regularized FE models of RVEs, compared a realistic microstructural morphology with the cuboidal morphology and reported that for relatively homogeneous microstructures, not much difference is obtained in the calculated values of RVE-averaged quantities and the distribution of grain-averaged quantities. Since in this work such volume-averaged quantities are calculated from the mesoscale model, the choice of a fixed cuboidal morphology is deemed reasonable.

The implementation of the material model along with the current microstructure model is verified by comparing the cycle-stabilized stress–strain curves predicted from the current implementation with the reference simulation results reported in [55].

# 4. Crack nucleation model

Different types of FIPs have been used in the literature to characterize the crack nucleation phenomenon, as reviewed in [10,44,45]. Amongst them, the critical-plane based Fatemi-Socie FIP has been

extensively used [47,49,50,52,53,57,87]. The Fatemi-Socie damage parameter was originally developed as a phenomenological concept applied to multiaxial fatigue and was an extension of the concept of critical planes responsible for fatigue damage [89]. In the past, the Fatemi-Socie parameter has been found to be representative of fundamental crack growth driving force parameters such as the stressintensity factor range, the  $\Delta J$ -integral, and the crack-tip displacement in slip bands [90–92]. It has also been found to correlate well with Stage I fatigue crack growth exhibiting planar slip [93]. Since for crack nucleation active slip planes can act as critical planes, Castelluccio and McDowell [94] extended the idea to introduce the Fatemi-Socie FIP for a crystal plasticity model. With this background, the Fatemi-Socie FIP is exploited in this work, which is expressed for the  $\alpha$ -th slip system and N-th loading cycle, as:

$$p_N^{\alpha} = \frac{\Delta \gamma_N^{\alpha}}{2} \left( 1 + k_{FS} \frac{\sigma_{n,N}^{\alpha}}{\sigma_{cyc}} \right)$$
 (10)

where,  $p_N^{\sigma}$  is the value of the FIP,  $\Delta \gamma_N^{\sigma}$  is the slip range and  $\sigma_{n,N}^{\sigma}$  is the peak normal stress.  $k_{FS}$  is the material parameter that governs the influence of normal stress. The value of  $k_{FS}$  for materials is typically obtained through identification on experiments [95], and in this work, a value of 1 is used, which is a value generally suggested for steels [95,96]. In a numerical model, the FIP, as expressed in Eq. (10), is calculated for an arbitrary volume of material which is governed by the modeling discretization scheme. Hence, this quantity can be affected by the choice of the discretization scheme of the numerical model. Moreover, this arbitrary volume may not be a physically realistic crack nucleating volume. To address these issues, the values of FIP are often volume-averaged over different choices of physically realistic domains that may represent the crack nucleating volume [81]. In this work, a grain-averaging scheme is adopted, as follows:

$$p_N^{\alpha,g} = \frac{\int_{V_g} p_N^{\alpha} dV_g}{V_{\sigma}} \tag{11}$$

in which  $V_g$  represents the volume of the g-th grain to which the arbitrary volumes belong and  $p_N^{\alpha,g}$  is the value of FIP for the combination of the g-th grain,  $\alpha$ -th slip system and N-th cycle. Such a grain-averaging scheme for FIPs has been used in the literature to characterize fatigue crack nucleation [47,72,87]. As observed by Castelluccio and McDowell [87], the grain-averaged FIP closely represents the FIP value existing at the mid-section of the grain. Since grain orientations are the primary microstructural features analyzed in this work, a single FIP value per slip system per grain is a reasonable choice. Moreover, given the choice of the cuboidal grain morphology used in this work, the grain-averaging scheme also reduces possible morphological edge effects in the calculated FIP value. Since  $p_N^{\alpha,g}$  evolves with loading cycles, only the characteristic cycle-stabilized value of FIP  $(p^{\alpha,g})$  is used for further calculation:

$$p^{\alpha,g} = p_{N_{es}}^{\alpha,g} \tag{12}$$

where,  $N_{ss}$  is the number of cycles needed to obtain a cyclic-stabilized state, defined as:

$$\left(\frac{\Delta p_N^{a,g}}{\Delta N} \to 0\right)_{N=N_{ss}} \tag{13}$$

This implicitly assumes that the number of cycles needed by a material to attain a stabilized state is significantly smaller than the number of cycles for crack nucleation. Thus, fatigue damage during the transient state can be neglected compared to the stabilized state fatigue damage

Table 3 Radii of the defects analyzed in this work and their corresponding  $K_r$  values.

r <sub>1</sub> [mm]	r <sub>2</sub> [mm]	K, [-]
1	1	3
1	0.68	4
1	0.5	5.2
1	0.25	9.7

(note that this assumption is not valid in the case of ultra-low-cycle fatigue). After obtaining  $p^{\alpha,g}$ , the associated maximum value ( $p_{max}$ ) for the considered mesoscale volume is evaluated as follows:

$$p_{max} = \max_{\alpha, g} (p^{\alpha, g}) \tag{14}$$

Based on the explanation in Section 2, the associated  $p_{max}$  value is represented by the random variable P and is used for predicting the crack nucleation life of the defect, as follows [94,96]:

$$N^n = \frac{p_{crit}}{(P)^{m_o}} \tag{15}$$

where,  $p_{crit}$  is a material parameter that depends on the grain size and irreversibility of dislocation activity [14,94]. The exponent  $m_o$  for the Fatemi-Socie FIP is often assigned the value of 2 [94,96].

# 5. Case study: Comparison of defects

This section presents the case study analyzed in this work which focuses on comparing different defects in a simple engineering structure for the prediction of their crack nucleation characteristics. First, the choices made for the geometry, FE strategies, and boundary conditions for the macroscale model of the structure and the mesoscale model of the microstructure are presented. Finally, the two-scale approach implemented using the two models is described, which enables the comparison of the defects.

# 5.1. Macroscale model

The macroscale FE model consists of a thick rectangular plate with a defect at the center of one of its long edges. A plane-strain deformation condition is assumed for the plate which is representative of the deformation conditions existing in the bulk of the structures. This assumption also makes it convenient to analyze the plate with a 2D FE model. Fig. 7 shows the 2D FE model of the plate along with its dimensions. The macroscale FE model is discretized with 8-noded plane strain quadrilateral elements CPE8. The considered defect in the plate is of a semi-elliptical cylinder shape, which, in a 2D plane-strain model, is modeled as a semi-ellipse. The shape of the defect is parametrized by the two radii:  $r_1$  and  $r_2$ , corresponding to the two semi-axes, as shown in the inset of Fig. 7. Four different defects with a fixed value of  $r_1 = 1$  mm and different values of  $r_2$  are analyzed in this work, resulting in four macroscale models. Mesh refinement is carried out in the vicinity of the defects with an average element size of about 10 µm, which is found to be sufficient for mesh-converged results for all the defects. The linear elastic stress concentration factors  $(K_t)$  of the defects, for plane strain conditions, based on the principal stress values in the direction of the semi-minor axis of the defect, are summarized in Table 3. Fig. 8 shows the close-ups of the four defects in their respective macroscale models.

The cyclic deformation of the plate is simulated by applying a cyclic load on its top edge, as shown in Fig. 7, with a maximum applied stress of  $\sigma_A$ = 122 MPa, a stress ratio of  $R_{\sigma,M}=-1$  and with a symmetrical triangular loading waveform. The value of  $\sigma_A$  is chosen as 90% of initial yield stress  $\sigma_{yo}$ . The cyclic load is applied for 25 cycles to reach a cyclestabilized stress–strain state in the vicinity of the defect. For the nodes located along the bottom edge, the displacement degree of freedom

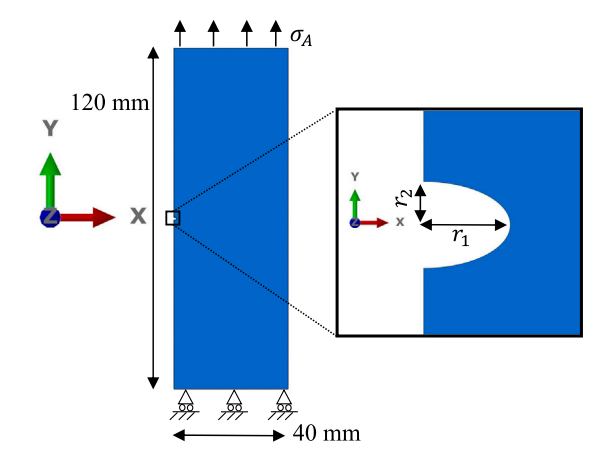
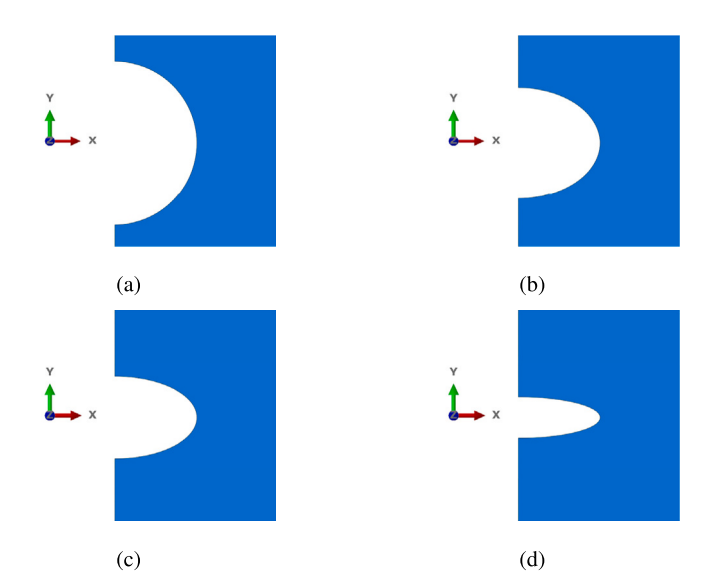


Fig. 7. Macroscale Model of a section of a thick plate with a defect, loaded in its plane. The two radii used to define the shape of the defect are shown in the inset.



**Fig. 8.** Close-ups on the defect of different  $K_t$  in their respective macroscale models: (a)  $K_t=3$  (b)  $K_t=4$  (c)  $K_t=5.2$  (d)  $K_t=9.7$ .

along the Y direction is constrained, thus allowing lateral contraction. A corner node on the bottom edge is constrained in X-direction to eliminate rigid body motion.

#### 5.2. Mesoscale model

The mesoscale FE model and the two-scale approach are implemented for a generic defect-root volume element of the material  $(v_m)$ around the central root point of the defect. Such  $v_m$  is shown schematically in Fig. 9. The reason for implementing the methodology for a generic defect-root volume elements is as follows: As discussed in Section 2, to compare different defects, mesoscale models for their associated DVEs are required, and for establishing the required DVE size, a size sensitivity needs to be conducted to address the two size criteria. Implementing the mesoscale FE model and the two-scale approach for a generic defect-root volume element enables such sensitivity studies. When  $v_m$  complies with the two size criteria, it serves as DVE for the defect, also shown schematically in Fig. 9. These size sensitivity studies are later discussed in Section 5.3. In the spirit of the explanations made in Section 2,  $v_m$  has a counterpart  $v_M$  in the macroscale model. The microstructure description used in the FE model of  $v_m$  is already described in Section 3.2. The coordinate system of the mesoscale FE

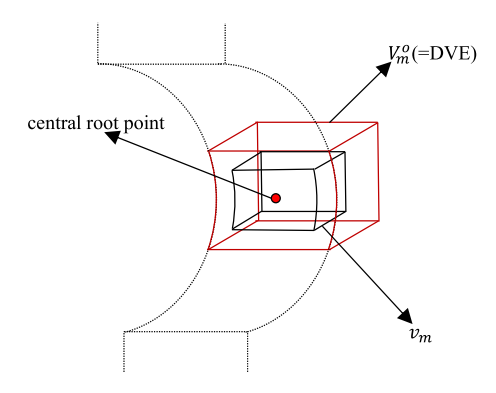


Fig. 9. Schematic diagram showing a generic defect-root volume element  $(v_m)$  and the required DVE  $(V_m^\circ)$  in the mesoscale model.

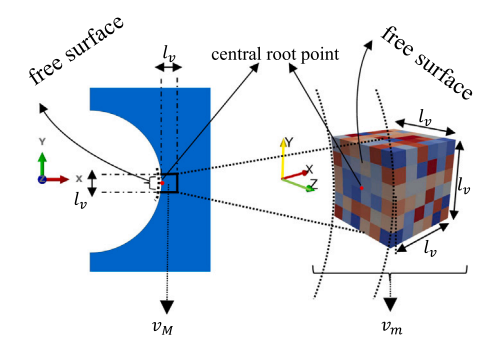


Fig. 10.  $v_M$  in macroscale model and  $v_m$  in mesoscale model for the case of  $K_t=3$  and  $n_{\rm g}=216.$ 

model of a defect is parallel to the coordinate system of the macroscale FE model of the defect, such that their central root points coincide. As an example, Fig. 10 shows  $v_m$  and  $v_M$  for the case  $K_t = 3$  and  $n_g = 216$ .

Each cuboidal grain in the FE model is discretized with 64 8-noded hexahedral elements, which is based on mesh-sensitivity studies. Since  $v_m$  is the volume of the material in the vicinity of the defect, apart from the microstructure of the material, the shape of the defect also plays a role in its description. Depending on the dimensions of the  $v_m$ , the mesoscale FE model of  $v_m$  incorporates a portion of the curved free surface of the defect. This is shown in Fig. 10, through the linear size of  $v_m$  ( $l_v$ ). The relationship between  $l_v$  and  $n_v$  is expressed as

$$l_v = d\sqrt[3]{n_g} \tag{16}$$

The boundary conditions are imposed on all enclosed surfaces of  $v_m$  (excluding the free surface), termed as the non-free surfaces of  $v_m$ . The displacement boundary conditions of the non-free surface of  $v_m$  are obtained from the last cycle results of the macroscale model. If  $\vec{d}_{max,m}(\vec{x})$  and  $\vec{d}_{max,M}(\vec{x})$  are the displacement vectors at the peak applied stress, of a point which has position vector  $\vec{x}$  with respect to the central root point of the defect in the mesoscale model and macroscale model respectively, the displacement vector of the non-free surface nodes of the mesoscale model reads:

$$\vec{d}_{max,m}(\vec{x}_m^n) = \vec{d}_{max,M}(\vec{x}_{2D,m}^n)$$
(17)

where  $\vec{x}_m^n$  denotes the position vector of a node at a non-free surface with respect to the central root point in the mesoscale model and  $\vec{x}_{2D,m}^n$  is its 2D projection in the plane of the macroscale model.  $\vec{x}_{2D,m}^n$  is mathematically expressed as:

$$\vec{\mathbf{x}}_{2D,m}^{n} = \left(\vec{\mathbf{x}}_{m}^{n} \cdot \vec{\mathbf{e}}_{x}\right) \vec{\mathbf{e}}_{x} + \left(\vec{\mathbf{x}}_{m}^{n} \cdot \vec{\mathbf{e}}_{y}\right) \vec{\mathbf{e}}_{y} \tag{18}$$

where  $\vec{e}_x$  and  $\vec{e}_y$  are the Cartesian unit base vectors of the coordinate system in the plane of the macroscale model. It is often found that the

extent of the local stress–strain reversal near the notch or defect root can be different from the globally applied stress–strain reversal [5,97]. To address this, a simple and easy-to-implement approach based on the average strain ratio is adopted. In this approach, the principal strain ratio for the mesoscale boundary conditions ( $R_{\varepsilon,m}$ ) is calculated from the results of the last cycle of the macroscale model as follows:

$$R_{\varepsilon,m} = \frac{\bar{\varepsilon}_{min,M}}{\bar{\varepsilon}_{max,M}} \tag{19}$$

where  $\bar{\varepsilon}_{min,M}$  and  $\bar{\varepsilon}_{max,M}$  denote the cycle minimum and cycle maximum values of the volume-averaged principal strain over the volume  $v_M$ . Thereafter, a displacement  $\vec{d}_{avg,m}(\vec{x}_m^n) \pm \left(\Delta \vec{d}_m(\vec{x}_m^n) \left| R_{\varepsilon,m} \right| \right)$  is imposed on the non-free surface nodes in the FE model to simulate cyclic loading of  $v_m$ , where:

$$\vec{d}_{avg,m}(\vec{x}_m^n) = \frac{\left(1 + R_{\varepsilon,m}\right)\vec{d}_{max,m}(\vec{x}_m^n)}{2} \tag{20}$$

$$\Delta \vec{d}_m(\vec{x}_m^n) = \frac{\left(1 - R_{\varepsilon,m}\right) \vec{d}_{max,m}(\vec{x}_m^n)}{2} \tag{21}$$

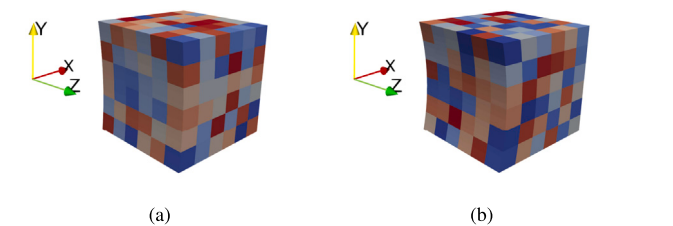
The average principal strain rate of the cyclic straining is kept at the value of  $0.002~\rm s^{-1}$ , which is the strain rate of the cyclic loading for which the material parameters were identified [55]. With the prescribed boundary conditions, the cyclic loading of  $v_m$  is carried out for 25 cycles to ensure the attainment of a cycle-stabilized volume-averaged stress–strain response, as well as cycle-stabilized  $p_N^{\alpha,g}$  values.

After simulating the cyclic loading of  $v_m$  for 25 cycles, the  $p_{max}$  value for a particular microstructure realization of  $v_m$  is calculated based on the methodology presented in Section 4. In order to remove the local influence of the boundary conditions, the grains residing at the non-free surface of  $v_m$  are not considered for the determination of  $p_{max}$ . Different  $p_{max}$  values are obtained for different microstructure realizations of  $v_m$ .

# 5.3. Two-scale implementation

The procedure of the two-scale approach to extract the distribution of the  $p_{max}$  values is outlined in Algorithm 1, where the number of microstructure realizations analyzed for a generic defect-root volume  $v_m$  of a defect is denoted by  $n_r$ . As explained before, to compare defects of different  $K_t$ , the distributions for  $p_{max}$  values corresponding to the DVEs are needed. The size of the DVE for the defects is identified by conducting a size-sensitivity study using Algorithm 1. In this work, the size of a DVE is established for the shallowest defect, i.e. the defect with  $K_t=3$ . As discussed in Section 2, the required DVE for this defect should satisfy the two size criteria: SC1 and SC2. Since the shallowest defect will have the lowest strain gradient in the two inplane directions, the established DVE for this defect is sufficient for studying other defects if it satisfies SC2, see Section 2, for all other defects.

For addressing SC1, a number of two-scale analyses are carried out using Algorithm 1, with  $r_1=1$  mm,  $r_2=1$  mm and  $n_r=50$ , each with a different  $v_m$  and hence a different value of  $n_g$ , ranging from  $27(=3\times3\times3)$  to  $343(=7\times7\times7)$ . From each of these two-scale analyses, the distribution of  $p_{max}$  values for each  $v_m$  is obtained and is characterized by estimating the associated mean ( $\mathbb{E}\left[p_{max}\right]$ ) and coefficient of variation ( $\mathbb{V}\left[p_{max}\right]$ ). It is observed that beyond  $n_g=216$ , a negligible change (<10%) in the estimated  $\mathbb{E}\left[p_{max}\right]$  and  $\mathbb{V}\left[p_{max}\right]$  are obtained for higher values of  $n_g$ , thereby confirming that SC1 is satisfied. Furthermore, for each defect, the cycle-stabilized volume-averaged stress–strain curves for  $v_m$  and  $v_m$  associated with  $n_g=216$  are in adequate agreement with each other, thereby satisfying SC2. Hence, it is concluded that for each defect, volume  $v_m$  with  $n_g=216$  qualifies to serve as a proper DVE. This results in a linear size of DVE,  $I_o=0.21$  mm for all the defects. The relative error associated with 95% confidence intervals of estimated



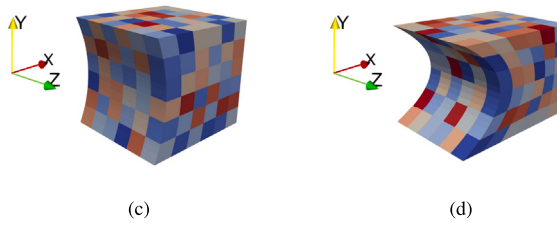


Fig. 11. The DVEs of defects with different  $K_t$ : (a)  $K_t = 3$  (b)  $K_t = 4$  (c)  $K_t = 5.2$  (d)  $K_t = 9.7$ .

# Algorithm 1: Procedure for the two-scale implementation.

Input : 
$$r_1$$
,  $r_2$ ,  $n_g$ ,  $n_r$ ,  $\left\{\Theta_1^r[n_g], \Theta_2^r[n_g], ...\Theta_{n_r}^r[n_g]\right\}$   
Output:  $\left\{p_{max,1}, p_{max,2}, ...p_{max,n_r}\right\}$ 

- <sup>1</sup> Set-up the macroscale FE model of the structure with  $r_1$  and  $r_2$
- 2 Simulate the macroscopic cyclic loading of the structure and store the results
- 3 Set-up the mesoscale FE model of j-th realization of  $v_m$  with  $r_1, r_2, \ n_g$  and  $\Theta_i^r[n_g]$
- 4 Extract the values of  $\vec{d}_{max,m}(\vec{x}_m^n)$  and  $R_{\varepsilon,m}$  from the results of the macroscale model
- 5 Simulate the mesoscale cyclic loading of  $v_m$
- 6 Extract the value of  $p_{max}$
- 7 Repeat Steps 3-6 for  $n_r$  realizations

 $\mathbb{E}\left[p_{max}\right]$  and  $\mathbb{V}\left[p_{max}\right]$ , expressed as twice the margin of error per unit estimated value, are calculated using the bootstrap method with 9999 resamples, and are found to be 5% and 42% respectively. The relative error associated with 95% confidence intervals indicates the error in the determination of the estimates [15] and is governed here by the sample size of  $p_{max}$ , and hence the number of realizations  $n_r$ . For this work, a value of  $n_r = 50$  is deemed sufficient to get estimates with reasonable accuracy within the constraints of computational resources. With the established values of  $n_g = 216$  and  $n_r = 50$  for DVEs of all the defects, Algorithm 1 is then further used to analyze different defects (different values of  $r_1$  and  $r_2$ ) for their associated  $p_{max}$  distribution, represented by the random variable  $P^{\circ}$ . The DVEs of defects with different values of  $K_t$  are shown in Fig. 11, where different colors denote different grains.

#### 6. Results and discussion

In this section, the results of the comparison of the defects are presented. First, the results of the distribution of predicted  $P^{\circ}$  and P for the defects are presented. Thereafter, the predicted trends of the distribution of  $N^n$  of defects are described. Finally, these trends are compared with the results of an empirical approach and experimental data sets.

# 6.1. Distribution of $P^{\circ}$ and P

To characterize the CDF of  $P^{\circ}$  of all defects, the Gumbel distribution is used. The Gumbel distribution is one of the extreme value distributions [98] and thus appropriate for characterizing the distribution of  $p_{max}$  in the vicinity of a defect. The Gumbel distribution has also been used in the literature for characterizing the maximum value of different types of FIPs of microstructures [15,49–51,71,81]. Using the Gumbel distribution, the CDF associated with  $P^{\circ}$  ( $F_{P^{\circ}}$ ) for a defect is expressed as [15,51]:

$$F_{P^{\circ}}(p; \mu^{\circ}, \sigma^{\circ}) = \exp\left[-\exp\left(-\frac{p - \mu^{\circ}}{\sigma^{\circ}}\right)\right]$$
 (22)

where p denotes a specific value of  $P^{\circ}$  and  $\mu^{\circ}$  and  $\sigma^{\circ}$  denote the location and scale parameter of the distribution, respectively.  $\mu^{\circ}$  and

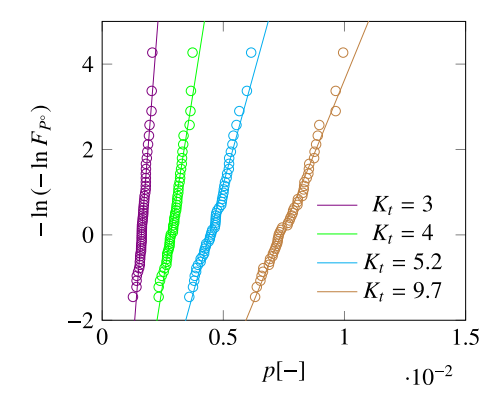


**Fig. 12.**  $P^{\circ}$  values calculated for defects of different  $K_t$  values, shown with open circles, and their Gumbel fit, shown with solid lines, plotted on the Gumbel probability scale.

**Table 4**Gumbel Parameters associated with  $P^{\circ}$  for different K.

	μ°[-]	σ°[-]
$K_t = 3$	0.0016	0.00014
$K_{t} = 4$	0.0028	0.00028
$K_t = 5.2$	0.0044	0.00049
$K_t = 9.7$	0.0074	0.00072

 $\sigma^{\circ}$  are collectively referred to as the Gumbel parameters. The Gumbel parameters of the four defect cases have been identified by the method of linearization and fitting, based on the procedure outlined in [50]. In summary, as per this procedure, Eq. (22) (also elsewhere) is expressed as:

$$-\ln\left(-\ln F_{P^{\circ}}\right) = \frac{p}{\sigma^{\circ}} - \frac{\mu^{\circ}}{\sigma^{\circ}} \tag{23}$$

which is a linear equation between  $-\ln\left(-\ln F_{P^\circ}\right)$  and p. Then, using the empirical values of  $F_{P^\circ}$  for different values of p, the values of  $\mu^\circ$  and  $\sigma^\circ$  are obtained by fitting the data to Eq. (23). Table 4 summarizes the values of Gumbel parameters obtained from the fitting procedure for the four defects, using the 50 values of  $P^\circ$  obtained from the two-scale analysis of their respective DVEs. Fig. 12 shows the Gumbel approximation graphically. A good match ( $R^2 > 0.95$ ) has been obtained for all defects. Based on the Gumbel parameters obtained, the probability density functions (PDF) associated with  $P^\circ$  ( $f_{P^\circ}$ ) for the defects are obtained, as shown in Fig. 13. The PDF of  $P^\circ$  shifts to higher values as the value of  $K_t$  increases. This is understandable since a defect with higher  $K_t$  has a higher driving force for crack nucleation [99]. It can also be observed that the standard deviation of  $p_{max}$  increases as  $K_t$  increases.

The  $p_{max}$  values associated with a defect of a particular shape and length  $(l_D)$  are represented by the random variable P. To obtain the distribution of P for defects of different lengths from the distribution of their corresponding  $P^\circ$ , a weakest link-based upscaling technique [15, 51,71], as discussed in Section 2, is used. Based on this approach, the CDF associated with P is estimated using Eq. (1), with  $n_\circ$  now expressed

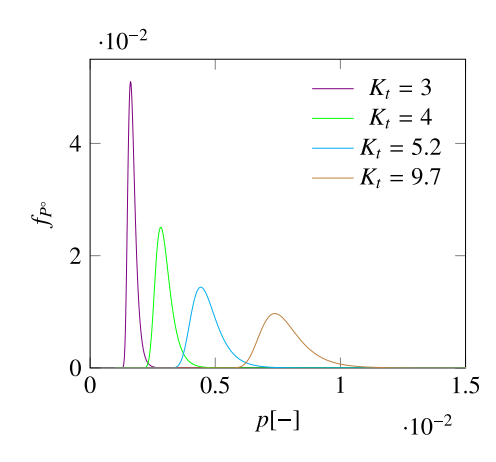


**Fig. 13.** Estimated PDF of  $P^{\circ}$  of defects with different  $K_{i}$  values.

as:

$$n_{\circ} = \frac{l_D}{l_{\circ}} \tag{24}$$

In terms of the Gumbel distribution of  $P^{\circ}$ , Eq. (1) is reformulated as [15,51]:

$$F_P(p; \mu^D, \sigma^D) = \exp\left[-\exp\left(-\frac{p - \mu^D}{\sigma^D}\right)\right]$$
 (25)

where

$$\mu^{D} = \left(\mu^{\circ} + \sigma^{\circ} \ln(n_{\circ})\right) \tag{26}$$

$$\sigma^D = \sigma^{\circ} \tag{27}$$

Eq. (25) shows that for a given defect P follows a Gumbel distribution with corresponding Gumbel parameters that depend on the Gumbel parameters of the associated  $P^{\circ}$ . Using Eq. (25),  $F_P$  is evaluated for three values of  $I_D$  for each value of  $K_t$  of a defect: 0.21 mm, 0.5 mm and 1 mm. The case of  $I_D = 0.21$  mm refers to the case where the defect is of the same size as DVE, i.e.  $n_o = 1$ . Fig. 14 shows  $F_P$  obtained for the defects with different values of  $I_D$  and  $K_t$ .

# 6.2. Distribution of $N^n$

Since P changes with  $K_t$  and  $l_D$ , it is denoted further as  $P_{K_t,l_D}$ . Similarly, using Eq. (15),  $N^n$  for a defect with a particular  $K_t$  and  $l_D$  is expressed as:

$$N_{K_{t},l_{D}}^{n} = \frac{p_{crit}}{\left(P_{K_{t},l_{D}}\right)^{m_{o}}} \tag{28}$$

Since  $P_{K_t,l_D}$  is a random variable, the term  $\frac{1}{\left(P_{K_t,l_D}\right)^{m_o}}$  is also a random variable. The term  $\frac{1}{\left(P_{K_t,l_D}\right)^{m_o}}$  is called unscaled crack nucleation life and is referred to with the symbol  $N^u_{K_t,l_D}$ . Eq. (28) is then rewritten as:

$$N_{K_{t},l_{D}}^{n} = p_{crit} N_{K_{t},l_{D}}^{u}$$
 (29)

The distribution of  $N^u_{K_t,l_D}$  depends on the distribution of  $P_{K_t,l_D}$ . For  $P_{K_t,l_D}$  that follows a Gumbel distribution with Gumbel parameters  $\mu^D$  and  $\sigma^D$ , the CDF for the  $N^u_{K_t,l_D}(F_{N^u})$ , based on the derivation in [15], is expressed as:

$$F_{N^u}(n; \mu^D, \sigma^D) = 1 - \exp\left[-\exp\left(-\frac{\left(\frac{1}{n}\right)^{m_o} - \mu^D}{\sigma^D}\right)\right]$$
(30)

where n denotes a specific value of  $N^u_{K_l,l_D}$ . The parameter  $p_{crit}$  is not available for pure  $\alpha$ -iron and hence Eq. (29) cannot be used directly.

Therefore, to compare the defects, two normalized crack nucleation lives  $(N_{K_l,l_D}^{n'})$  and  $N_{K_l,l_D}^{n''}$  are defined as follows:

$$N_{K_{t},I_{D}}^{n'} = \frac{N_{K_{t},I_{D}}^{n}}{\mathbb{E}\left[N_{K_{t}=3,I_{D}}^{n}\right]}$$
(31)

$$N_{K_{l},l_{D}}^{n''} = \frac{N_{K_{l}-3,l_{D}}^{n}}{\mathbb{E}\left[N_{K_{l}=3,l_{D}=0.21}^{n}\right]}$$
(32)

where  $\mathbb{E}\left[N_{K_i=3,I_D}^n\right]$  refers to the mean value of  $N_{K_i,I_D}^n$  for the defect with  $K_i=3$  and length  $=l_D$  and  $\mathbb{E}\left[N_{K_i=3,I_D=0.21}^n\right]$  refers to the mean value of  $N_{K_i,I_D}^n$  for the defect with  $K_i=3$  and  $I_D=0.21$ . Such normalized lives not only enable a relative comparison of the defects but also facilitate the prediction of the crack nucleation life of a particular defect, once the mean life has been identified from experimental data of the normalizing case. Eqs. (29), (31)–(32) show that  $N_{K_i,I_D}^u$ ,  $N_{K_i,I_D}^n$ , and  $N_{K_i,I_D}^{n''}$  are scaled versions of the actual  $N_{K_i,I_D}^n$  with different scaling factors. Using Eq. (29) and properties of the mean value of a random variable, Eq. (31) and (32) are rewritten as:

$$N_{K_{t},l_{D}}^{n'} = \frac{N_{K_{t},l_{D}}^{u}}{\mathbb{E}\left[N_{K_{t}=3,l_{D}}^{u}\right]}$$
(33)

$$N_{K_t,I_D}^{n''} = \frac{N_{K_t,I_D}^u}{\mathbb{E}\left[N_{K_t=3,I_D=0.21}^u\right]}$$
(34)

From Eq. (33), it is inferred that the Q-th quantile of  $N_{K_t,l_D}^{n'}$   $(F_{N^{n'}}^{-1}(Q))$  and Q-th quantile of  $N_{K_t,l_D}^{u}$   $(F_{N^{u}}^{-1}(Q))$  are related as follows:

$$F_{N^{n'}}^{-1}(Q) = \frac{F_{N^{u}}^{-1}(Q)}{\mathbb{E}\left[N_{K_{i}=3,I_{D}}^{u}\right]}$$
(35)

where  $F_{N^{n'}}^{-1}$  and  $F_{N^{u}}^{-1}$  are the inverse CDF of  $N_{K_{t},l_{D}}^{n'}$  and  $N_{K_{t},l_{D}}^{u}$  respectively. Similarly,

$$F_{N''}^{-1}(Q) = \frac{F_{N''}^{-1}(Q)}{\mathbb{E}\left[N_{K_i=3,I_D=0.21}^u\right]}$$
(36)

where  $F_{N^{n''}}^{-1}$  is the inverse CDF of  $N_{K_t,I_D}^{n''}$ . Using Eqs. (35) and (36) the first, second, and third quartiles of  $N_{K_t,I_D}^{n'}$  and  $N_{K_t,I_D}^{n''}$  are calculated using the quantile values of  $Q=0.25,\,0.5$  and 0.75, respectively, for each  $K_t$  and  $I_D$  value. These are then used to plot  $K_t$  vs  $N_{K_t,I_D}^{n'}$  and  $K_t$  vs  $N_{K_t,I_D}^{n''}$  in terms of interquartile ranges. The resultant graphs are shown in Figs. 15(a) and 15(b). Since both  $N_{K_t,I_D}^{n'}$  and  $N_{K_t,I_D}^{n''}$  are scaled versions of  $N_{K_t,I_D}^{n}$ , all the relative characteristics of the graph of  $K_t$  vs  $N_{K_t,I_D}^{n}$  on a log-log scale can be extracted from Figs. 15(a) and 15(b). A few observations are made from these figures regarding the variation of  $N_{K_t,I_D}^{n}$  with  $K_t$ :

- It is observed that for all  $l_D$ ,  $N_{K_t,l_D}^n$  decreases with an increase in  $K_t$ . This prediction is in line with the concept of stress concentration [4], which leads to early crack initiation in structures. Defects with higher  $K_t$  entail higher stresses and strain fields in the vicinity of the defect, which leads to higher values of P and lower values of  $N_{K_t,l_D}^n$ .
- $N_{K_t,l_D}^{n'}$  can be viewed as the life-reduction (or life debit) [100] which occurs when the value of  $K_t$  is increased for a particular value of  $l_D$ , expressed as a fraction of the life of the normalizing case. In this view, it is observed from Fig. 15(a), that the trend of life-reduction of  $N_{K_t,l_D}^n$  with  $K_t$  is nearly independent of  $l_D$ . Specifically, it is found that irrespective of  $l_D$ ,  $N_{K_t,l_D}^n$  reduces to about 5% of its value when  $K_t$  is increased from 3 to 9.7.

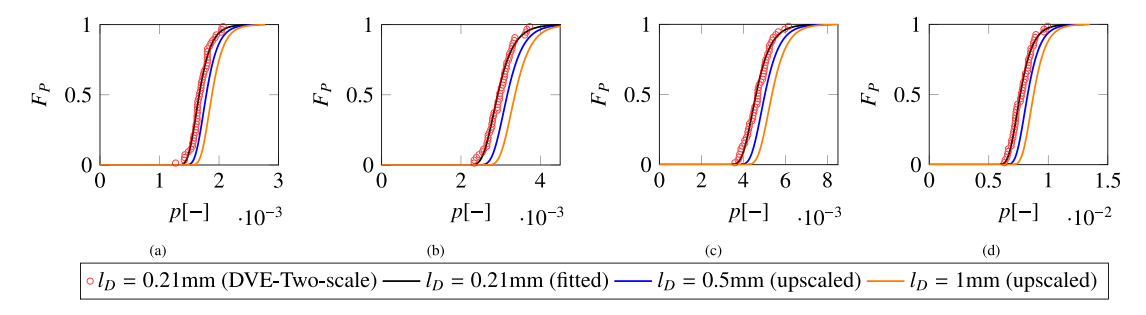


Fig. 14. CDF plots of P for different  $I_D$  values, obtained from the two-scale approach, fitting to Gumbel and statistical upscaling, for defects with different  $K_t$  values: (a)  $K_t = 3$  (b)  $K_t = 4$  (c)  $K_t = 5.2$  (d)  $K_t = 9.7$ .

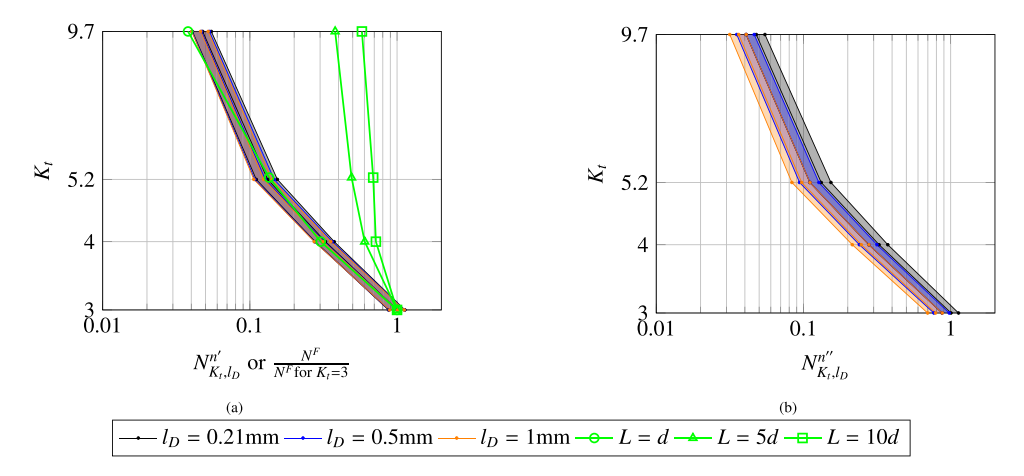


Fig. 15. Variation of different normalized lives with  $K_t$  values of defects: (a)  $N_{K_t,I_D}^{n'}$  obtained from two-scale approach for different  $l_D$  values and  $\frac{N^F}{N^F \text{ for } K_t=3}$  obtained from the Theory of critical distances with different values of L (b)  $N_{K_t,I_D}^{n''}$  obtained from two-scale approach for different  $l_D$  values.

- Fig. 15(b) reveals that for a particular  $K_t$ ,  $N_{K_t,l_D}^n$  decreases with increase in  $l_D$ . This is in line with the various types of size effects [101] which are typically observed in materials, wherein the fatigue strength or fatigue life of a material decreases with an increase of the fatigue-affected material volume [15,32,34]. In this work, this effect in the non-stress-gradient direction of a defect is captured by the statistics-based upscaling approach used. At a particular  $K_t$ , the defect with a higher  $l_D$  will have a higher fatigue crack nucleation-relevant material volume(=  $n_o \times \text{Volume}$  of DVE) in the vicinity of the defect, which increases the probability of finding a crack nucleating grain with a larger value of P. This eventually leads to a decrease in the mean (or median) crack nucleation life. Specifically, a reduction of about 21%–26% is observed in the median value of  $N_{K_t,l_D}^n$ , on increasing  $l_D$  from 0.21 to 1 mm, for all the  $K_t$  analyzed.
- It is observed that for a particular  $l_{\mathcal{D}}$  value, on a log–log scale, the spread of the interquartile range does not vary significantly with  $K_t$ . This is confirmed by calculating the coefficient of variation of  $N_{K,l_D}^n$  ( $\mathbb{V}[N^n]$ ) of all the defects. Since, as per Eq. (29),  $N_{K,l_D}^u$ is also a scaled version of  $N_{K,l_D}^n$ , the coefficient of variation of  $N^u_{K_t,l_D}$  is equal to  $\mathbb{V}[N^n]$ . Therefore  $\mathbb{V}[N^n]$  is calculated from a large sample that follows the CDF expressed in Eq. (30). Values of  $\mathbb{V}[N^n]$  calculated for different  $K_t$  and  $I_D$  are summarized in Table 5. For a particular  $l_D$  value, the  $\mathbb{V}[N^n]$  values do not differ significantly. This prediction is in line with the homoscedastic nature of the logarithm of the fatigue life of materials, which is often observed experimentally [102]. Experimentally, there is a large variation observed in the coefficient of variation of the fatigue life of materials, both in notched and un-notched conditions, ranging from as low as 0.1 to even more than 1 [26,102-106]. The values obtained here are on the lower side of this range. This likely relates to the fact that only one type of microstructural

**Table 5** Coefficient of variation of  $N^n$  for defects with different  $K_i$  and  $I_D$ .

		1 1
$l_D = 0.21 \text{ mm}$	$l_D = 0.5 \text{ mm}$	$l_D = 1 \text{ mm}$
0.19	0.18	0.17
0.22	0.20	0.19
0.24	0.22	0.21
0.21	0.20	0.19
	0.19 0.22 0.24	0.19 0.18 0.22 0.20 0.24 0.22

uncertainty is incorporated, i.e. the grain orientations, whereas experimentally there may be multiple factors contributing to the observed scatter [26,105]. The framework developed in this work can also be used to account for the microstructure-related uncertainty originating from the grain morphology and spatial arrangement, besides the texture. Assessment of the influence of morphology, spatial arrangement, and multiple phases is part of the future work.

• It is observed that, on a log-log scale,  $K_t$  vs  $N_{K_t,l_D}^n$  results in a nonlinear plot. Since all defects have the same depth in the direction of the principal stress gradient, i.e.  $r_1$ , this non-linear relationship is also reflected in a graph of the normalized local root radius of the defects versus  $N_{K_t,l_D}^{n'}$ . Normalized local root radius for a defect of a particular  $l_D$  is defined here as  $\frac{\rho}{\rho \text{ for } K_t=3}$ , where  $\rho$  is the local root radius of the defect, calculated as  $(r_2)^2/r_1$ . Such a graph is shown in Fig. 16(a). This predicted non-linear relationship between the root radius and  $N_{K_t,l_D}^n$  is in line with the experimentally reported nonlinear trend between the root radius of notches and observed  $N^I$  values [17,107,108]. Based on such a trend, it is often deduced that the influence of the local root radius of the notches on the fatigue life decreases with a decrease in root radius values [107,109]. This trend is also related

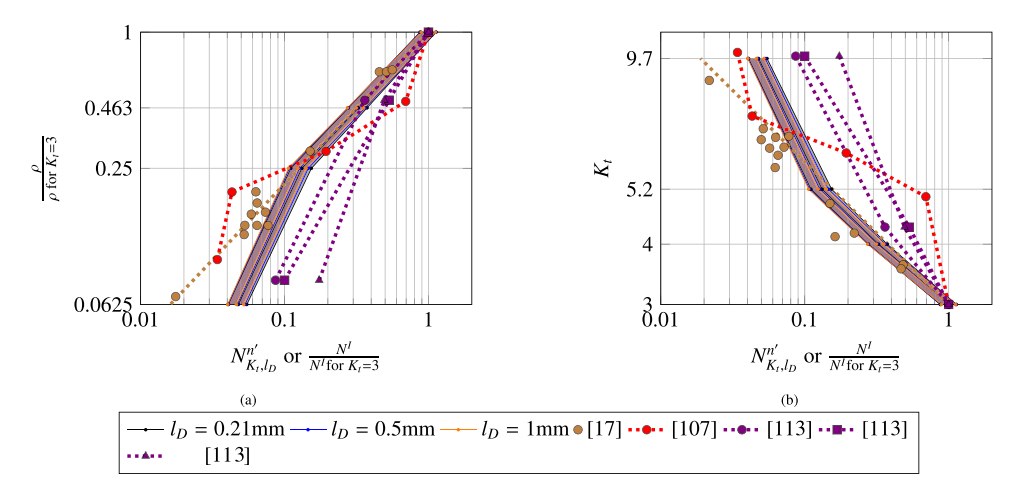


Fig. 16. Variation of life-reduction, obtained from two-scale approach  $(N_{K,I_D}^{nl})$  for different  $I_D$  values) and experiments  $(\frac{N^I}{N^I \text{for } K = 3})$ , with (a) normalized root-radius and (b)  $K_I$ .

to the observed phenomenon that the fatigue strength reduction by sharper notches is much less than that one would expect solely based on  $K_t$  [4,110]. There are many possible explanations given for this phenomenon such as the presence of local plasticity, stress gradient, etc [5]. In practice, this is often dealt with by introducing empirical formulations of the fatigue strength reduction factor [24,25]. In this work, the non-linearity between root radius and crack nucleation life is captured naturally and inherently by the combined effects of grain-level non-linear material behavior, rate dependency, and the grain-averaging scheme adopted to define the crack nucleation driving force.

### 6.3. Comparison with an empirical approach and experiments

The predictions of this model are first compared to the results obtained by applying the Theory of critical distances (TCD) [30,111], which is typically used to predict the fatigue life of notched components. The reason for choosing TCD as the method of comparison is that this method has been shown to predict the fatigue life of shallow to sharp notches with a reasonable degree of accuracy [30]. Specifically, the elastoplastic line-method version of TCD is used [30], as per which the fatigue life of the notch can be calculated using the following two equations of effective strain amplitude ( $\epsilon_{eff}$ ) and strain-life relationship:

$$\varepsilon_{eff} = \frac{1}{2L} \int_0^{2L} \varepsilon_a(r) dr \tag{37}$$

$$\varepsilon_{eff} = \frac{\sigma'_f}{F} (2N^F)^{bf} + \varepsilon'_f (2N^F)^{cf}$$
(38)

where  $\sigma'_f$ ,  $\varepsilon'_f$ ,  $b_f$ ,  $c_f$  are the strain-life parameters,  $\varepsilon_a(r)$  is the principal strain amplitude of a point in the macroscale model at a distance rfrom the central root point along the bisector of the defect, parallel to the semi-major axis, and L is the critical distance specific to the material of the study. L is a constant for the elastoplastic deformation case [30], and its value needs to be established from experimental fatigue life data of smooth and notched specimens. It is important to highlight that TCD falls under the category of non-mechanistic models [112] and the complete physical basis of L is still under study [112]. However, based on the compiled values of L related to different materials (metals and non-metals) and different properties of interest, it has been found that a reasonable range for values of L is between  $d^*$  and  $10d^*$  [111], where  $d^*$  is an underlying microstructural length scale, such as grain size. Hence in this work, three values of L are used, to simultaneously assess the sensitivity of the predictions by TCD to the values of L and to compare these predictions with the predictions of the two-scale approach. These values are L=d, 5d, and 10d. The

**Table 6** Strain-life parameters for pure  $\alpha$ -iron [73].

$\sigma'_f$ [MPa]	$\epsilon'_f$	$b_f$	$c_f$
630	0.14	-0.08	-0.44

values of  $\sigma'_f$ ,  $\varepsilon'_f$ ,  $b_f$ ,  $c_f$  for the case of pure  $\alpha$ -iron are extracted from the data given in [73], and are summarized in Table 6. Using this approach, for each value of L,  $N^F$  for different defects are estimated from the macroscale defect model and, analogous to  $N_{K_l,l_D}^{n'}$ , the life reduction is calculated as  $\frac{N^F}{N^F \text{for } K_t = 3}$ . This life reduction is compared with the prediction of the two-scale approach in Fig. 15(a). As can be observed from this figure the predictions of TCD are sensitive to the value of L, displaying a larger reduction in fatigue life for sharper defects for a smaller value of L. Note that an adequate agreement exists between the predictions of the case L = d and the predictions of the two-scale approach. This result resonates with the general observation that for fatigue in metallic materials, the value of L is of the order of the grain size [112]. It has also been observed by Taylor [112] that values of L in the order of the grain size imply that the failure mechanism is governed by the underlying microstructure. Note that, for the case L = d, the mean-stress corrected version of elastoplastic TCD [30] gives the same results as the one shown here, except for the case of  $K_t = 9.7$  where the mean-stress corrected version is more conservative and predicts a life-reduction that is 66% of the one presented here. The point method version of TCD is also assessed. However, it predicts nonrealistic results for higher values of L, wherein the normalized life is found to increase with  $K_t$ .

The authors have not found experimental values of crack nucleation lives for the same material and deformation conditions as the ones considered here. Nevertheless, five data sets are found that report  $N^I$  values, examined at low stress-amplitudes, for notched-specimen of low-carbon steels, having different values of root radius and thus  $K_t$  values [17,107,113]. The experimental conditions of these data sets are closest to the ones analyzed here of all data found in the literature. The salient details of materials and test conditions used in the data sets and those analyzed in this study are summarized in Table 7. For each data set, the life-reduction for a notch of a particular  $K_t$  is estimated as  $\frac{N^I}{N^I \text{for } K_t \approx 3}$ , where  $N^I \text{for } K_t \approx 3$  refers to  $N^I$  of the notch with  $K_t$  closest to 3. In the same way, normalized root radii are also calculated for different notches of a particular dataset. These life reductions along with their respective normalized root radii and  $K_t$  values are then plotted in the corresponding  $K_t$  vs Normalized root radius and  $K_t$  vs  $N_{N_t^{\prime\prime},D}^{\prime\prime}$  graphs of this study, respectively, as shown in Fig. 16.

It can be seen from both Figs. 16(a) and 16(b) that the data set from [17] shows a reasonable agreement with the predictions of the

Table 7

Comparison of material and testing conditions for the experimental data sets used in this work with the current case study.

	[17]	[107]	[113]	Current case study
Material	Carbon-Manganese	Mild-Steel	Deep-drawing steel	99.5% pure α-iron
	Steel			
YS (MPa)		214	185	200-250
UTS (MPa)		375	310	
E(GPa)		206	191	210
d(μm)	32	20		35
Specimen Type	Single Edged Notched	Single Edged Notched	Double edged notched	Thick Plate with
				defect on one edge
Notch/Defect Type		V-type	U and V type	Elliptical
Notch/Defect Depth (mm)	2	2.54	10	1
Notch Radius (mm)	0.02-2.54	0.05-1.27	0.1–10	0.0625-1
Κ,	3-10.7	3.82-15.18 (calculated)	3.24-9.81	3-9.7
Stress Amplitude (MPa)	82	103	89, 79, 59	122
Stress Ratio	0.3	0	0.1	-1
Initiation Criterion	0.1mm crack	Electric Potential Technique	0.5mm crack	Crack Nucleation

two-scale approach. For the data set of [107] as well, the experimental data points are scattered in reasonable proximity to the predicted curve in Fig. 16(a). In Fig. 16(b), the predictions are in reasonable proximity to experimental points of [107] at high  $K_t$  values, in comparison to low  $K_t$  values. All three data sets of [113] show smaller reduction in life compared to the predictions of the two-scale approach in both Figs. 16(a) and 16(b). A possible explanation is that the material studied in [113] was a high-ductility, low-notch-sensitive material. On comparing the reported values of monotonic and cyclic stress–strain, and strain-life parameters for this material in [113], with the respective reported values [73] of the pure  $\alpha$ -iron analyzed in this study, it follows that the material analyzed in [113] is less notch sensitive than the one analyzed here. Nevertheless, the predicted trend of variation of lifereduction with normalized root radius and  $K_t$  are generally in line with all five data sets.

# 7. Conclusions

In this work, a generalized two-scale approach is presented for addressing crack nucleation from macroscopic defects of different shapes and lengths while taking into account the local microstructural description in the vicinity of the defect. For a particular defect, the approach uses a macroscale model incorporating the geometrical description of the defect and several instantiations of mesoscale models to address the microstructural grain orientation variability in the vicinity of the defect. The cyclic deformation of the structure is modeled in the macroscale model to extract the strain fields in the vicinity of the defect, which are characteristic of the defect shape and material behavior at the macroscale. This strain field is then used to derive the boundary conditions for modeling the cyclic deformation in the mesoscale model. For the mesoscale model, the idea of a statistically representative defect-root volume element (DVE) is presented which enables the analysis of defects with different lengths embedded in the structure using a statistics-based upscaling approach. The cyclic deformation of the DVE of a defect is modeled under the extracted boundary conditions and the Fatemi-Socie fatigue indicator parameter, along with the associated crack nucleation model, is used to estimate the crack nucleation life of a defect. Using the established approach, multiple defects with different  $K_t$  values and lengths, in a plate of pure  $\alpha$ -iron material, are analyzed to assess the fatigue crack nucleation lives under plane strain conditions. The approach is found to inherently capture experimentally observed characteristics related to the fatigue life of defects without introducing any empirical factors, such as an inverse dependence on  $K_t$ , non-linear relationship with the local defectroot radius, homoscedastic nature, and size effects. Moreover, the trend of life-reduction with an increase in  $K_t$  values predicted by the current two-scale approach is found to be in adequate agreement with a prediction by the theory of critical distances. Finally, a comparison of the predictions is also made with five experimentally reported data

sets of different low-carbon steels. The predictions are found to be in reasonable quantitative agreement with most datasets and good qualitative agreement with all the datasets. Overall, the implemented approach is found to be promising and motivates further extension to structural steels.

# CRediT authorship contribution statement

Danish Khan: Writing – original draft, Validation, Software, Methodology, Formal analysis, Conceptualization. Davide Leonetti: Writing – review & editing, Supervision. Varvara G. Kouznetsova: Writing – review & editing, Supervision. Marc G.D. Geers: Writing – review & editing, Supervision. Johan Maljaars: Writing – review & editing, Supervision, Funding acquisition, Conceptualization.

# **Declaration of competing interest**

The authors declare that they have no known competing financial interests or personal relationships that could have appeared to influence the work reported in this paper.

# Data availability

Data will be made available on request.

# Acknowledgments

This research was carried out under project number T20006a in the framework of the Research Program of the Materials innovation institute (M2i) (www.m2i.nl) supported by Rijkswaterstaat and ProRail, Netherlands. This work used the Dutch national e-infrastructure with the support of the SURF Cooperative using grant no. EINF-5137. Thanks are also due to Mohammadreza Yaghoobi and Krzysztof S. Stopka for the support related to PRISMS Plasticity.

#### References

- Ostsemin AA, Utkin PB. Stress-concentration coefficients of internal welding defects. Russ Eng Res 2008;28(12):1165–8. http://dx.doi.org/10.3103/ \$1068798X08120034.
- [2] Becker WT, Shipley RJ, Aliya D. Use of the term defect. J Failure Anal Prev 2005;5:16–20. http://dx.doi.org/10.1361/15477020522915.
- [3] Rogerson JH. Defects in welds: Their prevention and their significance. In: Burgess NT, editor. Quality assurance of welded construction. 2nd ed.. CRC Press; 1989, p. 129-48. http://dx.doi.org/10.1201/9781482296501.
- [4] Dieter GE, Bacon D. Mechanical Metallurgy. McGraw-Hill Book Company (UK) Limited; 1988.
- [5] Bannantine JA, Comer JJ, Handrock JL. Fundamentals of Metal Fatigue Analysis. Englewood Cliffs, New Jersey 07632: Prentice Hall; 1990.
- [6] McDowell DL. Basic issues in the mechanics of high cycle metal fatigue. Int J Fract 1996;80:103–45. http://dx.doi.org/10.1007/BF00012666.

- [7] Suresh S, Ritchie RO. Propagation of short fatigue cracks. Int Met Rev 1984;29(1):445–75. http://dx.doi.org/10.1179/imtr.1984.29.1.445.
- [8] McDowell DL, Gall K, Horstemeyer MF, Fan J. Microstructure-based fatigue modeling of cast A356-T6 alloy. Eng Fract Mech 2003;70(1):49–80. http://dx. doi.org/10.1016/S0013-7944(02)00021-8.
- [9] McDowell DL. Microstructure-sensitive modeling and simulation of fatigue. In: Furrer DU, Semiatin SL, editors. In: Fundamentals of modeling for metals processing, vol. 22A, ASM International; 2009, p. 408–18. http://dx.doi.org/ 10.31399/asm.hb.v22a.a0005405.
- [10] McDowell DL, Dunne FPE. Microstructure-sensitive computational modeling of fatigue crack formation. Int J Fatigue 2010;32(9):1521–42. http://dx.doi.org/ 10.1016/j.ijfatigue.2010.01.003.
- [11] Pineau A, McDowell DL, Busso EP, Antolovich SD. Failure of metals II: Fatigue. Acta Mater 2016;107:484–507. http://dx.doi.org/10.1016/j.actamat.2015.05.
- [12] Laird C, Krause AR. A theory of crack nucleation in high strain fatigue. Int J Fract Mech 1968;4:219–31. http://dx.doi.org/10.1007/BF00185258.
- [13] Lin TH, Ito YM. Fatigue crack nucleation in metals. Proc Natl Acad Sci 1969;62(3):631–5. http://dx.doi.org/10.1073/pnas.62.3.631.
- [14] Tanaka K, Mura T. A dislocation model for fatigue crack initiation. J Appl Mech 1981;48(1):97–103. http://dx.doi.org/10.1115/1.3157599.
- [15] Gu T, Stopka KS, Xu C, McDowell DL. Modeling the statistical distribution of fatigue crack formation lifetime in large volumes of polycrystalline microstructures. Acta Mater 2023;247:118715. http://dx.doi.org/10.1016/j.actamat.2023. 118715.
- [16] Ishihara S, McEvily AJ. On the early initiation of fatigue cracks in the high cycle regime. In: Proceedings of the 12th international conference on fracture. 2009, p. On CD-ROM.
- [17] Allery MBP, Birkbeck G. Effect of notch root radius on the initiation and propagation of fatigue cracks. Eng Fract Mech 1972;4(2):325–31. http://dx. doi.org/10.1016/0013-7944(72)90047-1.
- [18] Ranganathan N, Aldroe H, Lacroix F, Chalon F, Leroy R, Tougui A. Fatigue crack initiation at a notch. Int J Fatigue 2011;33(3):492–9. http://dx.doi.org/ 10.1016/j.iifatigue.2010.09.007.
- [19] Chan KS. Roles of microstructure in fatigue crack initiation. Int J Fatigue 2010;32(9):1428–47. http://dx.doi.org/10.1016/j.ijfatigue.2009.10.005.
- [20] Mazánová V, Heczko M, Polák J. On the mechanism of fatigue crack initiation in high-angle grain boundaries. Int J Fatigue 2022;158:106721. http://dx.doi. org/10.1016/j.ijfatigue.2022.106721.
- [21] Atzori B, Lazzarin P. Notch sensitivity and defect sensitivity under fatigue loading: Two sides of the same medal. Int J Fract 2001;107:1–8. http://dx. doi.org/10.1023/A:1007686727207.
- [22] Dowling NE. Mechanical behavior of materials-engineering methods for deformation, fracture, and fatigue. Pearson Education Limited, Harlow, Essex, England; 2013.
- [23] Liao D, Zhu S-P, Correia JAFO, De Jesus AMP, Berto F. Recent advances on notch effects in metal fatigue: A review. Fatigue Fract Eng Mater Struct 2020;43(4):637–59. http://dx.doi.org/10.1111/ffe.13195.
- [24] Peterson RE. Notch sensitivity. In: Sines G, Waisman JL, editors. Metal fatigue. McGraw-Hill, New York; 1959, p. 293–306.
- [25] Neuber H. Kerbspannungslehre: Theorie der spannungskonzentration genaue berechnung der festigkeit. Springer Berlin, Heidelberg; 2001, http://dx.doi.org/ 10.1007/978-3-642-56793-3.
- [26] Schijve J. Fatigue of structures and materials. Springer Dordrecht; 2009, http://dx.doi.org/10.1007/978-1-4020-6808-9.
- [27] Neuber H. Theory of stress concentration for shear-strained prismatical bodies with arbitrary nonlinear stress-strain law. J Appl Mech 1961;28(4):544–50. http://dx.doi.org/10.1115/1.3641780.
- [28] Molski K, Glinka G. A method of elastic-plastic stress and strain calculation at a notch root. Mater Sci Eng 1981;50(1):93–100. http://dx.doi.org/10.1016/0025-5416(81)90089-6.
- [29] Fatemi A, Zeng Z, Plaseied A. Fatigue behavior and life predictions of notched specimens made of QT and forged microalloyed steels. Int J Fatigue 2004;26(6):663–72. http://dx.doi.org/10.1016/j.ijfatigue.2003.10.005.
- [30] Susmel L, Taylor D. An elasto-plastic reformulation of the theory of critical distances to estimate lifetime of notched components failing in the low/medium-cycle fatigue regime. J Eng Mater Technol 2010;132(2):021002. http://dx.doi.org/10.1115/1.4000667.
- [31] Susmel L, Taylor D. A novel formulation of the theory of critical distances to estimate lifetime of notched components in the medium-cycle fatigue regime. Fatigue Fract Eng Mater Struct 2007;30(7):567–81. http://dx.doi.org/10.1111/ j.1460-2695.2007.01122.x.
- [32] Kuguel R. A relation between theoretical stress concentration factor and fatigue notch factor deduced from the concept of highly stressed volume. In: American society for testing and materials proceedings, vol. 61, 1961, p. 732–48.
- [33] Rennert R, Kullig E, Vormwald M, Esderts A, Luke M. FKM-Richtlinie rechnerischer festigkeitsnachweis. 7 auflage. Frankfurt/Main: VDMA-Verlag; 2020.
- [34] Liao D, Zhu S-P, Keshtegar B, Qian G, Wang Q. Probabilistic framework for fatigue life assessment of notched components under size effects. Int J Mech Sci 2020;181:105685. http://dx.doi.org/10.1016/j.ijmecsci.2020.105685.

- [35] Meggiolaro MA, Castro JTP. Statistical evaluation of strain-life fatigue crack initiation predictions. Int J Fatigue 2004;26(5):463–76. http://dx.doi.org/10. 1016/i.iifatigue.2003.10.003.
- [36] Castillo E, Fernández-Canteli A, Pinto H, López-Aenlle M. A general regression model for statistical analysis of strain-life fatigue data. Mater Lett 2008;62(21–22):3639–42. http://dx.doi.org/10.1016/j.matlet.2008.04.015.
- [37] Baldwin JD, Thacker JG. A strain-based fatigue reliability analysis method. J Mech Des 1995;117(2A):229–34. http://dx.doi.org/10.1115/1.2826127.
- [38] Chan KS. A microstructure-based fatigue-crack-initiation model. Metall Mater Trans A 2003;34:43–58. http://dx.doi.org/10.1007/s11661-003-0207-9.
- [39] Sangid MD. The physics of fatigue crack initiation. Int J Fatigue 2013;57:58–72. http://dx.doi.org/10.1016/j.ijfatigue.2012.10.009.
- [40] Krupp U, Düber O, Christ H-J, Künkler B, Schick A, Fritzen C-P. Application of the EBSD technique to describe the initiation and growth behaviour of microstructurally short fatigue cracks in a duplex steel. J Microsc 2004;213(3):313–20. http://dx.doi.org/10.1111/j.0022-2720.2004.01306.x.
- [41] Brückner-Foit A, Huang X. Numerical simulation of micro-crack initiation of martensitic steel under fatigue loading. Int J Fatigue 2006;28(9):963–71. http://dx.doi.org/10.1016/j.ijfatigue.2005.08.011.
- [42] Dunne FPE. Fatigue crack nucleation: Mechanistic modelling across the length scales. Curr Opin Solid State Mater Sci 2014;18(4):170–9. http://dx.doi.org/10. 1016/j.cossms.2014.02.005.
- [43] Mlikota M, Schmauder S, Bozic Z. Multiscale fatigue modelling of metals. In: Dogahe KJ, editor. In: Materials research foundation, vol. 114, Millersville, PA, USA: Materials Research Forum LLC; 2022, p. 1–88. http://dx.doi.org/10. 21741/9781644901656.
- [44] Segurado J, Lebensohn RA, LLorca J. Computational homogenization of polycrystals. Adv Appl Mech 2018;51:1–114. http://dx.doi.org/10.1016/bs.aams. 2018.07.001.
- [45] P. Jirandehi A, M. Khonsari M. General quantification of fatigue damage with provision for microstructure: A review. Fatigue Fract Eng Mater Struct 2021;44(8):1973–99. http://dx.doi.org/10.1111/ffe.13515.
- [46] Manonukul A, Dunne FPE. High-and low-cycle fatigue crack initiation using polycrystal plasticity. Proc R Soc Lond Ser A Math Phys Eng Sci 2004;460(2047):1881-903. http://dx.doi.org/10.1098/rspa.2003.1258.
- [47] Shenoy M, Zhang J, McDowell DL. Estimating fatigue sensitivity to polycrystalline Ni-base superalloy microstructures using a computational approach. Fatigue Fract Eng Mater Struct 2007;30(10):889–904. http://dx.doi.org/10.1111/j.1460-2695.2007.01159.x.
- [48] Przybyła CP, McDowell DL. Simulated microstructure-sensitive extreme value probabilities for high cycle fatigue of duplex Ti-6Al-4V. Int J Plast 2011;27(12):1871-95. http://dx.doi.org/10.1016/j.ijplas.2011.01.006.
- [49] Sharaf M, Kucharczyk P, Vajragupta N, Munstermann S, Hartmaier A, Bleck W. Modeling the microstructure influence on fatigue life variability in structural steels. Comput Mater Sci 2014;94:258–72. http://dx.doi.org/10.1016/j.commatsci.2014.05.059.
- [50] Przybyla CP, McDowell DL. Microstructure-sensitive extreme value probabilities for high cycle fatigue of Ni-base superalloy IN100. Int J Plast 2010;26(3):372–94. http://dx.doi.org/10.1016/j.ijplas.2009.08.001.
- [51] Gu T, Stopka KS, Xu C, McDowell DL. Prediction of maximum fatigue indicator parameters for duplex Ti-6Al-4V using extreme value theory. Acta Mater 2020;188:504-16. http://dx.doi.org/10.1016/j.actamat.2020.02.009.
- [52] Stopka KS, McDowell DL. Microstructure-sensitive computational multiaxial fatigue of Al 7075-T6 and duplex Ti-6Al-4V. Int J Fatigue 2020;133:105460. http://dx.doi.org/10.1016/j.ijfatigue.2019.105460.
- [53] Lakshmanan A, Yaghoobi M, Stopka KS, Sundararaghavan V. Crystal plasticity finite element modeling of grain size and morphology effects on yield strength and extreme value fatigue response. J Mater Res Technol 2022;19:3337–54. http://dx.doi.org/10.1016/j.jmrt.2022.06.075.
- [54] Guerchais R, Saintier N, Morel F, Robert C. Micromechanical investigation of the influence of defects in high cycle fatigue. Int J Fatigue 2014;67:159–72. http://dx.doi.org/10.1016/j.ijfatigue.2014.01.005.
- [55] Briffod F, Shiraiwa T, Enoki M. Microstructure modeling and crystal plasticity simulations for the evaluation of fatigue crack initiation in α-iron specimen including an elliptic defect. Mater Sci Eng A 2017;695:165–77. http://dx.doi. org/10.1016/j.msea.2017.04.030.
- [56] Cui C, Xu Y-L, Zhang Q-H. Multiscale fatigue damage evolution in orthotropic steel deck of cable-stayed bridges. Eng Struct 2021;237:112144. http://dx.doi. org/10.1016/j.engstruct.2021.112144.
- [57] Owolabi GM, Prasannavenkatesan R, McDowell DL. Probabilistic framework for a microstructure-sensitive fatigue notch factor. Int J Fatigue 2010;32(8):1378–88. http://dx.doi.org/10.1016/j.ijfatigue.2010.02.003.
- [58] Musinski WD, McDowell DL. Microstructure-sensitive probabilistic modeling of HCF crack initiation and early crack growth in Ni-base superalloy IN100 notched components. Int J Fatigue 2012;37:41–53. http://dx.doi.org/10.1016/ j.ijfatigue.2011.09.014.
- [59] Li L, Shen L, Proust G. Fatigue crack initiation life prediction for aluminium alloy 7075 using crystal plasticity finite element simulations. Mech Mater 2015;81:84–93. http://dx.doi.org/10.1016/j.mechmat.2014.11.004.

- [60] Dabiri M, Lindroos M, Andersson T, Afkhami S, Laukkanen A, Björk T. Utilizing the theory of critical distances in conjunction with crystal plasticity for lowcycle notch fatigue analysis of S960 MC high-strength steel. Int J Fatigue 2018;117:257–73. http://dx.doi.org/10.1016/j.ijfatigue.2018.07.042.
- [61] Li K-S, Cheng L-Y, Xu Y, Wang R-Z, Zhang Y, Zhang X-C, et al. A dual-scale modelling approach for creep-fatigue crack initiation life prediction of holed structure in a nickel-based superalloy. Int J Fatigue 2022;154:106522. http://dx.doi.org/10.1016/j.ijfatigue.2021.106522.
- [62] Bishop JE, Emery JM, Field RV, Weinberger CR, Littlewood DJ. Direct numerical simulations in solid mechanics for understanding the macroscale effects of microscale material variability. Comput Methods Appl Mech Engrg 2015;287:262–89. http://dx.doi.org/10.1016/j.cma.2015.01.017.
- [63] Stopka KS, Yaghoobi M, Allison JE, McDowell DL. Simulated effects of sample size and grain neighborhood on the modeling of extreme value fatigue response. Acta Mater 2022;224:117524. http://dx.doi.org/10.1016/j.actamat. 2021.117524.
- [64] Diehl M, Shanthraj P, Eisenlohr P, Roters F. Neighborhood influences on stress and strain partitioning in dual-phase microstructures: An investigation on synthetic polycrystals with a robust spectral-based numerical method. Meccanica 2016;51:429–41. http://dx.doi.org/10.1007/s11012-015-0281-2.
- [65] Abdolvand H, Wright J, Wilkinson AJ. Strong grain neighbour effects in polycrystals. Nature Commun 2018;9(1):171. http://dx.doi.org/10.1038/s41467-017-02213-9.
- [66] Ball JA, Kareer A, Magdysyuk OV, Michalik S, Connolley T, Collins DM. Revealing per-grain and neighbourhood stress interactions of a deforming ferritic steel via three-dimensional X-ray diffraction. Commun Mater 2024;5(1):27. http://dx.doi.org/10.1038/s43246-024-00466-8.
- [67] Noor AK. Global-local methodologies and their application to nonlinear analysis. Finite Elem Anal Des 1986;2(4):333–46. http://dx.doi.org/10.1016/0168-874X(86)90020-X.
- [68] Ransom JB, Knight Jr NF. Global/local stress analysis of composite panels. Comput Struct 1990;37(4):375–95. http://dx.doi.org/10.1016/0045-7949(90) 90027-Y.
- [69] Cook RD. Finite element modeling for stress analysis. 1st ed.. USA: John Wiley & Sons, Inc.; 1994.
- [70] Zhou J, Zhang GQ. Introduction to advanced mechanics. In: Zhang GQ, Van Driel WD, Fan XJ, editors. Mechanics of microelectronics. Dordrecht: Springer; 2006, p. 95–167. http://dx.doi.org/10.1007/1-4020-4935-8\_4.
- [71] Lucarini S, Segurado J. An upscaling approach for micromechanics based fatigue: From RVEs to specimens and component life prediction. Int J Fract 2020;223(1):93–108. http://dx.doi.org/10.1007/s10704-019-00406-5.
- [72] Briffod F, Shiraiwa T, Enoki M. Fatigue crack initiation simulation in pure iron polycrystalline aggregate. Mater Trans 2016;57(10):1741–6. http://dx.doi.org/ 10.2320/matertrans.M2016216.
- [73] Briffod FRL. Microstructure-sensitive modeling for the prediction of fatigue performances in structural steels (Ph.D. thesis), University of Tokyo; 2017.
- [74] Takeda K, Nakada N, Tsuchiyama T, Takaki S. Effect of interstitial elements on Hall—Petch coefficient of ferritic iron. ISIJ Int 2008;48(8):1122–5. http: //dx.doi.org/10.2355/isijinternational.48.1122.
- [75] Lopez Z, Fatemi A. A method of predicting cyclic stress-strain curve from tensile properties for steels. Mater Sci Eng A 2012;556:540–50. http://dx.doi.org/10. 1016/j.msea.2012.07.024.
- [76] Hartloper AR, de Castro e Sousa A, Lignos DG. Constitutive modeling of structural steels: Nonlinear isotropic/kinematic hardening material model and its calibration. J Struct Eng 2021;147(4):04021031. http://dx.doi.org/10.1061/ (ASCE)ST.1943-541X.0002964.
- [77] Sajjad HM, Hanke S, Güler S, ul Hassan H, Fischer A, Hartmaier A. Modelling cyclic behaviour of martensitic steel with J2 plasticity and crystal plasticity. Materials 2019;12(11). http://dx.doi.org/10.3390/ma12111767.
- [78] Franciosi P, Le LT, Monnet G, Kahloun C, Chavanne MH. Investigation of slip system activity in iron at room temperature by SEM and AFM in-situ tensile and compression tests of iron single crystals. Int J Plast 2015;65:226–49. http://dx.doi.org/10.1016/j.ijplas.2014.09.008.
- [79] Kalidindi SR. Polycrystal plasticity: Constitutive modeling and deformation processing [Ph.D. thesis], Massachusetts Institute of Technology; 1992.
- [80] Yaghoobi M, Ganesan S, Sundar S, Lakshmanan A, Rudraraju S, Allison JE, et al. PRISMS-Plasticity: An open-source crystal plasticity finite element software. Comput Mater Sci 2019;169:109078. http://dx.doi.org/10.1016/j.commatsci. 2019.109078.
- [81] Yaghoobi M, Stopka KS, Lakshmanan A, Sundararaghavan V, Allison JE, McDowell DL. PRISMS-Fatigue computational framework for fatigue analysis in polycrystalline metals and alloys. npj Comput Mater 2021;7(1):38. http://dx.doi.org/10.1038/s41524-021-00506-8.
- [82] Bangerth W, Hartmann R, Kanschat G. Deal.II—A general-purpose objectoriented finite element library. ACM Trans Math Softw 2007;33(4):24–es. http://dx.doi.org/10.1145/1268776.1268779.

- [83] Frederick CO, Armstrong PJ. A mathematical representation of the multiaxial Bauschinger effect. Mater High Temp 2007;24(1):1–26. http://dx.doi.org/10. 1179/096034007X207589
- [84] Böhlke T. Crystallographic texture evolution and elastic anisotropy: Simulation, modeling, and applications. Aachen: Shaker Verlag. 2001.
- [85] Bachmann F, Hielscher R, Schaeben H. Texture analysis with MTEX-free and open source software toolbox. Solid State Phenomena 2010;160:63–8. http: //dx.doi.org/10.4028/www.scientific.net/ssp.160.63.
- [86] Benedetti I, Barbe F. Modelling polycrystalline materials: An overview of three-dimensional grain-scale mechanical models. J Multiscale Model 2013;5(01):1350002. http://dx.doi.org/10.1142/S1756973713500029.
- [87] Castelluccio GM, McDowell DL. Microstructure and mesh sensitivities of mesoscale surrogate driving force measures for transgranular fatigue cracks in polycrystals. Mater Sci Eng A 2015;639:626–39. http://dx.doi.org/10.1016/j. msea.2015.05.048.
- [88] Sauzay M, Liu J, Rachdi F, Signor L, Ghidossi T, Villechaise P. Physically-based simulations of the cyclic behavior of FCC polycrystals. In: 11th international fatigue congress. Advanced materials research, vol.891, Trans Tech Publications Ltd; 2014, p. 833–9. http://dx.doi.org/10.4028/www.scientific.net/AMR.891-892.833.
- [89] Fatemi A, Socie DF. A critical plane approach to multiaxial fatigue damage including out-of-phase loading. Fatigue Fract Eng Mater Struct 1988;11(3):149–65. http://dx.doi.org/10.1111/j.1460-2695.1988.tb01169.x.
- [90] Reddy SC, Fatemi A. Small crack growth in multiaxial fatigue. In: Mitchell MR, Landgraf RW, editors. Advances in fatigue lifetime predictive techniques. ASTM International; 1992, p. 276–98. http://dx.doi.org/10.1520/STP24164S.
- [91] McDowell DL, Berard J-Y. A \( \Delta \J\)-based approach to biaxial fatigue. Fatigue Fract Eng Mater Struct 1992;15(8):719-41. http://dx.doi.org/10.1111/j.1460-2695.1992.tb00053.x.
- [92] Castelluccio GM, McDowell DL. Assessment of small fatigue crack growth driving forces in single crystals with and without slip bands. Int J Fracture 2012;176:49–64. http://dx.doi.org/10.1007/s10704-012-9726-y.
- [93] Socie D, Marquis G. Multiaxial fatigue. SAE International; 1999.
- [94] Castelluccio GM, McDowell DL. Mesoscale modeling of microstructurally small fatigue cracks in metallic polycrystals. Mater Sci Eng A 2014;598:34–55. http: //dx.doi.org/10.1016/j.msea.2014.01.015.
- [95] Shamsaei N, Fatemi A. Effect of hardness on multiaxial fatigue behaviour and some simple approximations for steels. Fatigue Fract Eng Mater Struct 2009;32(8):631–46. http://dx.doi.org/10.1111/j.1460-2695.2009.01369.x.
- [96] Natkowski E, Durmaz AR, Sonnweber-Ribic P, Münstermann S. Fatigue lifetime prediction with a validated micromechanical short crack model for the ferritic steel EN 1.4003. Int J Fatigue 2021;152:106418. http://dx.doi.org/10.1016/j. ijfatigue.2021.106418.
- [97] Wang CH, Rose LRF. Transient and steady-state deformation at notch root under cyclic loading. Mech Mater 1998;30(3):229-41. http://dx.doi.org/10. 1016/S0167-6636(98)00048-9.
- [98] Castillo E. Extreme value theory in engineering. Elsevier; 1988, http://dx.doi. org/10.1016/C2009-0-22169-6.
- [99] Tanaka K, Mura T. A micromechanical theory of fatique crack initiation from notches. Mech Mater 1982;1(1):63–73. http://dx.doi.org/10.1016/0167-6636(82)90024-2.
- [100] Sobotka JC, Enright MP, McClung RC. Application of critical distances to fatigue at pores. Fatigue Fract Eng Mater Struct 2019;42(8):1646-61. http: //dx.doi.org/10.1111/ffe.13004.
- [101] Kloos KH. Einfluß des oberflächenzustandes und der probengröße auf die schwingfestigkeitseigenschaften. VDI-Ber 1976;268:63–76.
- [102] Wirsching PH. Statistical summaries of fatigue data for design purposes. Technical report, NASA; 1983.
- [103] Sasaki SK, Ochi Y, Ishii A, Abe H. Effects of material structures on statistical scatter in initiation and growth lives of surface cracks and failure life in fatigue. JSME Int J Ser 1, Solid Mech, Strength Mater 1989;32(1):155–61. http://dx.doi.org/10.1299/jsmea1988.32.1\_155.
- [104] Tryon RG, Cruse TA. Probabilistic mesomechanical fatigue crack nucleation model. J Eng Mater Technol 1997;119(1):65–70. http://dx.doi.org/10.1115/1. 2805975.
- [105] Schijve J. Fatigue predictions and scatter. Fatigue Fract Eng Mater Struct 1994;17(4):381–96. http://dx.doi.org/10.1111/j.1460-2695.1994.tb00239.x.
- [106] Strzelecki P, Mazurkiewicz A, Musiał J, Tomaszewski T, Słomion M. Fatigue life for different stress concentration factors for stainless steel 1.4301. Materials 2019;12(22):3677. http://dx.doi.org/10.3390/ma12223677.
- [107] Jack AR, Price AT. The initiation of fatigue cracks from notches in mild steel plates. Int J Fract Mech 1970;6:401–9. http://dx.doi.org/10.1007/BF00182628.
- [108] Saanouni K, Bathias C. Study of fatigue crack initiation in the vicinity of notches. Eng Fract Mech 1982;16(5):695–706. http://dx.doi.org/10.1016/0013-7944(82)90023-6.

- [109] Coffin LF. Fatigue crack initiation at notches Techniques, experiments and interpretations. In: Branco CM, Rosa LG, editors. Advances in fatigue science and technology. Netherlands, Dordrecht: Springer; 1989, p. 417–44. http://dx.doi.org/10.1007/978-94-009-2277-8\_18.
- [110] Frost NE, Marsh KJ, Pook LP. Metal fatigue. Courier Corporation; 1999.
- [111] Taylor D. The theory of critical distances: A link to micromechanisms. Theor Appl Fract Mech 2017;90:228–33. http://dx.doi.org/10.1016/j.tafmec.2017.05. 018.
- [112] Taylor D. The theory of critical distances: A new perspective in fracture mechanics. Elsevier, Linacre House, Jordon Hill, Oxford, UK, 2007: Elsevier; 2007, http://dx.doi.org/10.1016/B978-0-08-044478-9.X5000-5.
- [113] Lazzarin P, Tovo R, Meneghetti G. Fatigue crack initiation and propagation phases near notches in metals with low notch sensitivity. Int J Fatigue 1997;19(8–9):647–57. http://dx.doi.org/10.1016/S0142-1123(97)00091-1.